

Max Planck Institute for Physics

Fakultät für Physik  
Technische Universität München

A thesis

submitted in partial fulfillment of the requirements for the degree of

Master of Science

in

Nuclear, Particle and Astrophysics

# Bayesian Analysis of the First Data of the KATRIN Experiment

MARTIN HA MINH

OCTOBER 30, 2018

Supervisor: Prof. Dr. Susanne Mertens



Max-Planck-Institut für Physik





## Erklärung

Ich versichere hiermit, dass ich diese Masterarbeit selbstständig verfasst und nur die angegebenen Quellen und Hilfsmittel verwendet habe.

---

Martin Ha Minh



## Abstract

Neutrino oscillations prove that neutrinos have a mass and provide a means to determine the squared mass difference between neutrino mass eigenstates. However, their absolute mass scale is still unknown. A neutrino mass model independent approach to measure the absolute neutrinos mass scale is based on the kinematics of the  $\beta$ -decay. The Mainz and Troitsk neutrino mass experiments currently provide the best upper limit on the effective electron antineutrino mass of  $2 \text{ eV}/c^2$ .

The KARlsruhe TRItium Neutrino (KATRIN) Experiment is designed to improve the sensitivity by one order of magnitude to  $200 \text{ meV}/c^2$  (90% C.L.). It investigates the tritium  $\beta$ -decay close to the kinematic endpoint of the energy spectrum with a high-resolution electrostatic spectrometer ( $\Delta E = 0.93 \text{ eV}$  at  $18.6 \text{ keV}$ ).

This thesis is focused on the analysis of two data sets: (1) from a calibration campaign using the full beamline in summer 2018 using a gaseous  $^{83\text{m}}\text{Kr}$  source and (2) from our first measurement using gaseous tritium in spring 2017, setting the final preparations for the neutrino mass measurement campaign next year.

In this work we investigate the usage of the powerful Bayesian Analysis Toolkit (BAT), which was developed at the Max-Planck-Institute for Physics. In particular our studies focus on the aspect of, firstly, how to combine the data of different pixels of the 148 channel focal plane detector, and secondly, how to include systematic uncertainties in the fit using the Bayesian school of data analysis. We also compare different priors and their influence on our model selection. As a result, we demonstrate a very good agreement of the model and the data and in particular we establish the applicability of BAT for the KATRIN data analysis.



# Contents

<b>1</b>	<b>Neutrino Physics</b>	<b>3</b>
1.1	Postulation and Discovery of Neutrino . . . . .	3
1.2	Neutrino Oscillations . . . . .	3
1.3	Determining the Absolute Neutrino Mass . . . . .	4
<b>2</b>	<b>The KATRIN Experiment</b>	<b>7</b>
2.1	Experimental Setup . . . . .	7
2.2	Modelling the Response Function . . . . .	9
<b>3</b>	<b>Statistics</b>	<b>14</b>
3.1	Choice of Likelihood . . . . .	14
3.2	Bayesian School of Analysis . . . . .	14
3.3	Bayesian Analysis Toolkit . . . . .	16
<b>4</b>	<b>Strategies for Handling the Structure of the Focal Plane Detector</b>	<b>17</b>
4.1	Single-Pixel Fits . . . . .	17
4.2	Uniform Fits . . . . .	17
4.3	Multi-Pixel Fits . . . . .	18
<b>5</b>	<b>The Gaseous <math>^{83\text{m}}\text{Kr}</math> Source in the KATRIN Experiment</b>	<b>21</b>
5.1	Decay and Line Model . . . . .	21
5.2	Analysis of the $L_{3-32}$ Line . . . . .	24
5.3	Discussion of Systematic Uncertainties . . . . .	30
5.4	Estimating the Energy Resolution of the KATRIN Experiment . . . . .	32
<b>6</b>	<b>First Tritium Data</b>	<b>35</b>
6.1	Description of the Tritium Spectrum . . . . .	35
6.2	Likelihood Function . . . . .	38
6.3	Analysis of the First Tritium Data . . . . .	38
6.4	Discussion of Systematic Uncertainties . . . . .	47

<b>7 Conclusion</b>	<b>55</b>
7.1 Outlook . . . . .	56
<b>Appendices</b>	<b>58</b>
<b>A Additional Content Concerning the Krypton Analysis</b>	<b>59</b>
A.1 Settings . . . . .	59
A.2 Discussion of Systematic Uncertainties . . . . .	60
A.3 Multi-Pixel Fits . . . . .	61
<b>B Additional Content Concerning the Tritium Analysis</b>	<b>62</b>
B.1 Prior Probability Distribution Functions for $m_\nu^2$ . . . . .	62
B.2 Settings . . . . .	63
B.3 Multi-Pixel Fits . . . . .	64
B.4 Treatment of Systematic Uncertainties . . . . .	65

# Chapter 1

## Neutrino Physics

First, we want to shortly illustrate the history of the neutrino. We recount the postulation and discovery of the neutrino and its different flavors. Next, we depict the journey of neutrino oscillation studies and the proof of the existence of the neutrino mass. We also compile methods for determining the absolute mass of the neutrino.

### 1.1 Postulation and Discovery of Neutrino

The neutrino was first proposed by Wolfgang Pauli [Pau] in 1930. Considering the knowledge at that time, the  $\beta$ -decay seemed to be violating multiple conservation laws; e.g. for the assumed two-body decay, a fixed energy for the beta electron would be expected; instead a continuous energy spectrum was observed. Pauli postulated the neutrino, that would be emitted alongside with the electron and hence share the decay energy. Later, Enrico Fermi published his work *Theory of  $\beta$ -decay* in 1934 where he formulated the decay involving the neutrino and lent it its name [Fer34].

In 1956 the neutrino, specifically the electron antineutrino, was finally proven to exist by Cowan and Reines with an approach using inverse  $\beta$ -decay [Cow+56]. Subsequent experiments also showed that other neutrino flavors exist: the muon neutrino by Schwartz, Ledermann, and Steinberger in 1962 [Dan+62] and the tau neutrino by the DONUT experiment in 2000 [Kod+01].

### 1.2 Neutrino Oscillations

The Homestake experiment [DHH68] [Cle+98] in the 1970s discovered the *solar neutrino problem*: compared to the expected flux of electron neutrinos from the sun, they could only detect a fraction of that. Many other experiments confirmed the same problem. Pontecorvo earlier, along with his theoretical description of the neutrino mass and flavor eigenstates, predicted a mechanism with which neutrinos could change their flavors based

on their energy and distance traveled, the neutrino oscillation [Pon58]:

The mass eigenstate of the neutrino is a superposition state of the flavor eigenstates and vice-versa:

$$\begin{aligned} |\nu_i\rangle &= \sum_{\alpha} U_{\alpha i} |\nu_{\alpha}\rangle, \\ |\nu_{\alpha}\rangle &= \sum_i U_{\alpha i}^* |\nu_i\rangle. \end{aligned} \tag{1.1}$$

Where  $|\nu_i\rangle$  and  $|\nu_{\alpha}\rangle$  are neutrino mass and flavor eigenstates respectively, and  $U_{\alpha i}$  and  $U_{\alpha i}^*$  are the Pontecorvo–Maki–Nakagawa–Sakata matrix elements [MNS62] and their complex conjugates. And for the propagation of a mass eigenstate:

$$|\nu_i(t)\rangle = e^{iE_i t} |\nu_i\rangle. \tag{1.2}$$

The probability for a flavor state transition is then:

$$P_{\alpha \rightarrow \beta} = \langle \nu_{\beta}(t) | \nu_{\alpha} \rangle = \sum_{i,j} U_{\alpha i}^* U_{\beta i} U_{\alpha j} U_{\beta j}^* \exp\left(-i \frac{\Delta m_{ij}^2 L}{2E}\right), \tag{1.3}$$

where  $\Delta m_{ij}^2 = m_i^2 - m_j^2$  is the squared neutrino mass difference,  $L$  is the distance traveled by the neutrino, and  $E$  is its energy. This means for neutrino oscillations to occur, at least one mass eigenvalue has to be different from the others, and consequently, at least one mass eigenvalue has to be non-zero.

Super-Kamiokande [Hos+06] and the SNO experiment [Ahm+01] later demonstrated the existence of neutrino oscillations, and effectively showed that neutrinos need to have a mass. Many experiments afterwards studied neutrino oscillations and their parameters. However from neutrino oscillations we can only deduce the mixing angles as well as the mass squared differences, but not the absolute mass scale and their ordering.

## 1.3 Determining the Absolute Neutrino Mass

For the measurement of the absolute neutrino mass scale, different approaches exist. We present a non-exhaustive list with a short description of their methods.

### 1.3.1 Cosmology

The  $\Lambda$ CDM is the cosmological model that describes the universe according to the Big Bang. Based on the cosmic microwave background data combined with large-scale structure formation observations the neutrino mass can be deduced. The imprint of a neutrino mass on these cosmological probes is based on the fact that neutrinos act as hot dark matter and thus wash out small scales structures in our cosmos. The *Planck* observations

set the limit of the neutrino mass eigenstate sum to  $\sum_i m_i < 0.23$  eV [P A+16]. This approach is however highly model dependent.

### 1.3.2 Neutrinoless Double Beta Decay

A property that is still unknown about the neutrino is whether it is a Dirac or a Majorana particle, the latter implying it is its own antiparticle. A Majorana neutrino would allow the so-called neutrinoless double beta decay:

$$(A, Z) \rightarrow (A, Z + 2) + 2e^- \quad (1.4)$$

In the decay spectrum of the electron energies this would manifest itself in a sharp peak at the  $Q$ -value of the decay. The decay rate of this mechanism is proportional to the effective Majorana mass of the electron neutrino  $m_{\beta\beta}$ :

$$\Gamma_{0\nu\beta\beta} = G|M|^2|m_{\beta\beta}|^2 \quad (1.5)$$

With  $G$  the two-body phase-space factor and  $M$  the nuclear matrix element. The most stringent limit on the effective Majorana mass at the moment is set by the KamLAND-Zen experiment with upper limits in the range of 61 – 165 meV [Gan+16]. This approach makes the assumption however that the neutrino is indeed a Majorana particle; in addition the nuclear matrix element is accompanied by a large uncertainty.

### 1.3.3 Tritium Beta Decay

A neutrino mass model independent approach to determine the absolute neutrino mass is the measurement of the kinematics of the  $\beta$ -decay near the endpoint. A massive neutrino, no matter how small its mass, leaves a small shape distortion in the spectrum that can be measured:

$$\frac{d\Gamma}{dE} \propto \sum_i |U_{ei}|^2 \sqrt{E_\nu^2 - m_i^2} \quad (1.6)$$

Equation (1.6) shows the relation of the neutrino mass eigenstates  $m_i$  with the  $\beta$ -decay. We will discuss it in detail in section 6.1. By accurately measuring the spectrum, it is possible to make statements about the effective electron neutrino mass  $m_\nu = \sum_i |U_{ei}|^2 m_i$ . Using this approach, the Mainz [Kra+05] and Troitsk [Ase+11] neutrino mass experiments have set the upper limit of the effective electron antineutrino mass to 2 eV/ $c^2$  [Tan+18]. This is also the method the KATRIN experiment pursues. Fig. 1.1 shows the  $\beta$ -decay spectrum and fig. 1.2 shows the signature of different effective electron neutrino masses.

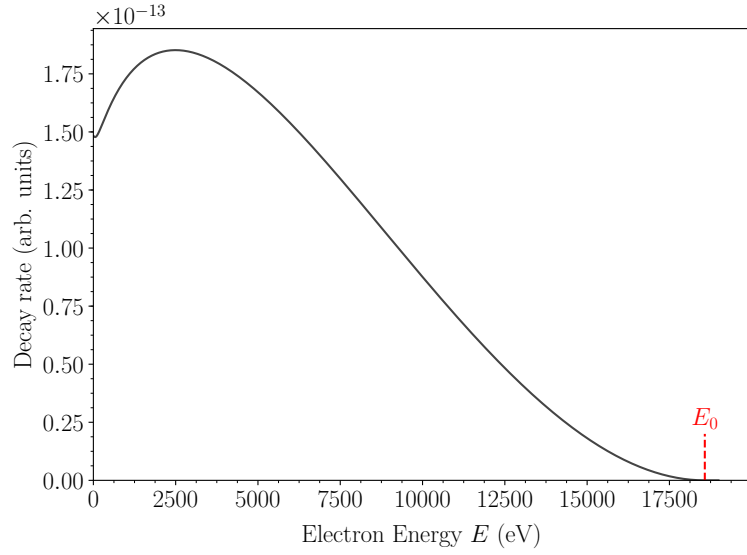


Figure 1.1:  $\beta$ -decay spectrum with the endpoint  $E_0$ , i.e. the maximum energy a beta electron can assume with  $m_\nu = 0$ .

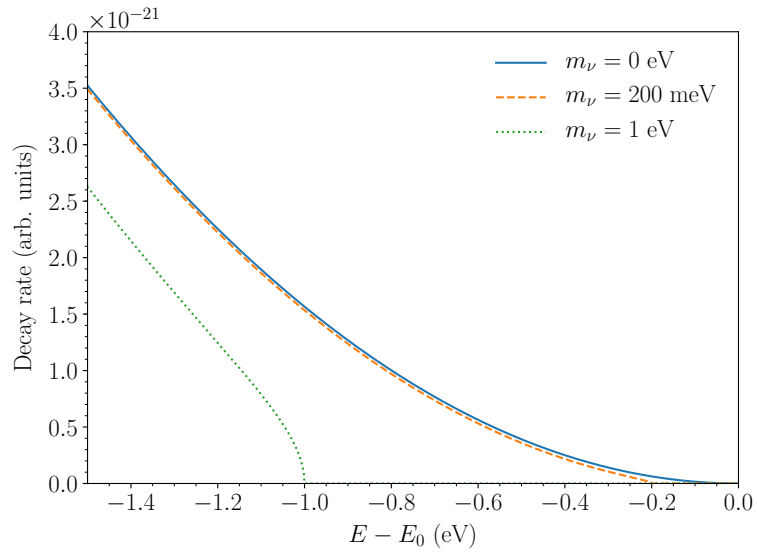


Figure 1.2: Zoom into the endpoint region of  $\beta$ -decay spectra for different effective electron neutrino masses  $m_\nu$  for  $c = 1$ .

## Chapter 2

# The KATRIN Experiment

The Karlsruhe TRItium Neutrino (KATRIN) Experiment is designed to improve the sensitivity of the effective electron antineutrino mass by one order of magnitude to  $200 \text{ meV}/c^2$  (90% C.L.). It investigates the tritium  $\beta$ -decay close to the kinematic endpoint of the energy spectrum with the combination of a high luminosity gaseous tritium source and a high-resolution electrostatic spectrometer [KK05].

### 2.1 Experimental Setup

In the following an overview of the most important parts of the KATRIN experiment and their function in the setup is displayed. Fig. 2.1 shows a schematic view of the experimental setup.

**Rear Section** The rear section [Bab14] is located at one end of the KATRIN experimental setup. A gold plated rear wall defines the starting electrical potential for the electrons.

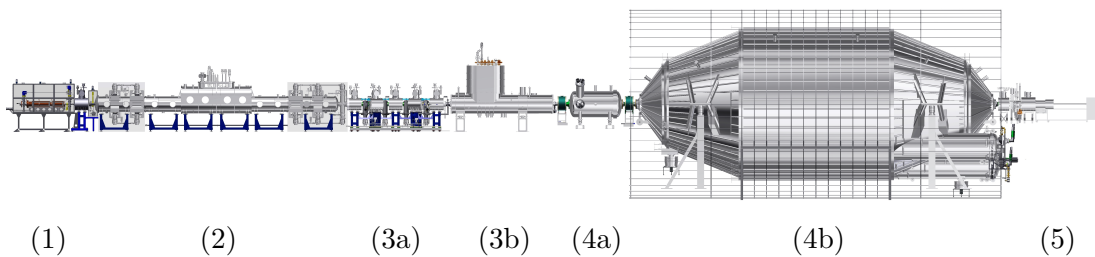


Figure 2.1: A schematic view of the KATRIN experimental setup. The shown elements are (1) the rear section, (2) the Windowless Gaseous Tritium Source (WGTS), (3a) the Differential Pumping Section and (3b) the Cryogenic Pumping Section, (4a) the Pre-Spectrometer and (4b) the Main Spectrometer, and (5) the detector section.

Additionally it is equipped with monitoring and calibration tools, such as an electron gun for the measurement of the electron energy loss function [Beh+17].

**Windowless Gaseous Tritium Source** The 10 m long Windowless Gaseous Tritium Source (WGTS) [Ha17] contains the tritium for the experimental analysis. The name stems from its design; windows would increase the electron scattering greatly, which, in this design, is eliminated. The tritium gas in the source is composed of its isotopologues T<sub>2</sub>, DT and HT; however the main component is T<sub>2</sub> with a purity of 95%. The tritium produces approximately 10<sup>11</sup> decays per second, which has to be kept at a relative stability of 10<sup>-3</sup> per hour. The WGTS is therefore equipped with tritium loops, which extract, clean, and reintroduce the gas continuously. The source is operated at a temperature of 30 K and a target column density of 5 · 10<sup>17</sup>cm<sup>-2</sup>.

**Transport Section** The tritium gas has to be removed before entering the spectrometer section to reduce contamination and background. This happens in the transport section, comprised of two pumping systems: the Differential Pumping Section (DPS) and the Cryogenic Pumping Section (CPS).

The DPS [Luo+06] [Luk+12] is equipped with four turbomolecular pumps to reduce the tritium flow initially by a factor of 10<sup>5</sup>. Additionally, five superconducting magnets at 5.6 T guide the electrons through the beam tube. These are tilted at angles so that the tritium molecules cannot travel in a straight line through the setup.

The CPS [Gil+10] reduces the tritium flow by another factor of 10<sup>7</sup>. Similarly to the DPS, the CPS has seven superconducting magnets to guide the electrons from the source through the kinked beam line. The beam tubes are covered with argon frost at 4 K where the tritium gas condenses. As the molecules accumulate, the frost layer has to be replaced regularly by heating and flushing the section.

**Spectrometer Section** The spectrometer section is comprised of two spectrometers, the pre-spectrometer and the main spectrometer. Both work under the MAC-E filter (Magnetic Adiabatic Collimation with Electrostatic filter) principle [LS85][Pic+92]. We discuss this further in section 2.2.1. Additionally they operate under ultra-high-vacuum with < 10<sup>-10</sup> mbar to reduce electron scattering inside.

The role of the pre-spectrometer [FW03] [Bor06] is to pre-filter electrons before they enter the main spectrometer. In the neutrino mass measurement the information is contained in the spectrum of electrons with an energy close to the endpoint. Electrons below that threshold can be filtered out. These electrons could otherwise ionize residual gas in the main spectrometer and consequently produce additional background, so it is desirable for them to be filtered before.

The main analysis happens in the 23 m long and 10 m wide main spectrometer [Val06]. Depending on the set high voltage the electrons either pass the potential barrier or get

reflected and lost. By setting the spectrometer to different voltages and observing the electron rate, the integral  $\beta$ -spectrum is recorded.

**Detector Section** The Focal Plane Detector (FPD) [Ams+15] counts the electrons that pass the experimental setup. It is a silicon based PIN diode detector with a dead layer of 100 nm, a radius of 4.5 cm, and is segmented in 148 pixels of equal area.

The detector section exhibits many features to maximize the signal from the  $\beta$ -decay electrons. Although mostly used as a counting detector, it also has an energy resolution of 1.4 keV at Full Width Half Maximum (FWHM). This can be used to apply energy cuts to reject background counts. It is additionally cooled down to  $-30^\circ\text{C}$  to reduce electrical noise. Both passive and active shielding minimize the impact from cosmic rays or surrounding radioactivity. Lastly, a post acceleration electrode in front of the detector accelerates the electrons coming from the main spectrometer.

The pixelation allows for the localization of the measured counts. We can simulate which electrons travel which parts of the experiment and arrive on which pixel. Based on their trajectory the electrons experience slightly different electromagnetic fields. We take this into account by applying *field maps*, which we obtain by the particle tracking simulation software Kassiopeia [Fur+17].

## 2.2 Modelling the Response Function

An electron that is emitted from the source with an energy  $E$  can, with a certain probability, pass the experiment and get detected at the end. This probability is described by the so-called response function  $R$ . The differential spectrum  $S$  with which the electrons are emitted is then observed as the integrated spectrum  $I$ :

$$I(qU) = \int_{-\infty}^{+\infty} S(E) \cdot R(E, qU) \, dE. \quad (2.1)$$

$I(qU)$  denotes the count rate at the retarding potential  $qU$ . For a perfect high energy pass filter, the response function would be a Heaviside step function at the retarding potential  $qU$ . However due to physical limitations, the response function must be expressed differently. This is discussed in this section.

### 2.2.1 MAC-E Filter Spectroscopy

The main spectrometer exploits the MAC-E filter principle: Two solenoid magnets at each side of the spectrometer form an axially symmetric inhomogeneous magnetic field. Electrons are emitted and enter from one end. The magnetic field lines then guide them into the spectrometer in a cyclotronic motion. On the way from the entrance to the center, the magnetic field drops by a factor of 20000. This leads to a transformation of the

perpendicular momentum component into the parallel one. As the change of the magnetic field during one cyclotron revolution is small, this transformation can be seen as adiabatic; therefore the magnetic moment  $\mu$  is constant:

$$\mu = (\gamma + 1) \cdot \frac{E_{\perp}}{B} = \text{const}, \quad (2.2)$$

for the transverse kinetic energy  $E$ , the magnetic field  $B$  and the relativistic gamma factor  $\gamma = E/m_e + 1$ . Inside the spectrometer, an electric field with the voltage  $U$  is applied. Its maximum value is at the center of the spectrometer, which coincides with the minimum magnetic field  $B_A$ . This central plane is called the analyzing plane. There, almost all of the kinetic energy of the electron is transformed into the parallel component, which is used to overcome the electric potential barrier. Electrons with a parallel kinetic energy higher than  $qU$  pass the electrostatic barrier, get reaccelerated, and focused onto the detector. Electrons with a lower parallel kinetic energy are reflected and generally lost.

From eq. (2.2) we obtain the relative energy resolution of the MAC-E filter:

$$\frac{\Delta E}{E} = \frac{B_A}{B_{\max}} \cdot \frac{\gamma + 1}{2} \quad (= 0.93 \text{ eV at } 18.6 \text{ keV design value}). \quad (2.3)$$

The MAC-E filter can in principle collect and analyze all electrons emitted into a  $2\pi$  solid angle. However, electrons with large emission angles exhibit large travel distances and therefore have a higher scattering probability inside the source. To minimize this effect, only electrons with an emission angle smaller than the acceptance angle  $\theta_{\max}$  may enter the spectrometer. This is achieved by surrounding the source with a magnetic field  $B_S < B_{\max}$ . The maximum acceptance angle is then:

$$\theta_{\max} = \arcsin \sqrt{\frac{B_S}{B_{\max}}} \quad (= 51^\circ \text{ design value}). \quad (2.4)$$

The transmission function for an ideal MAC-E filter with an isotropically emitting electron source and maximum acceptance angle  $\theta_{\max}$  is then given by:

$$T(E, qU) = \begin{cases} 0 & \text{for } E - qU < 0, \\ \frac{1 - \sqrt{1 - \frac{E - qU}{E} \frac{B_S}{B_A} \frac{2}{\gamma + 1}}}{1 - \sqrt{1 - \frac{B_S}{B_{\max}}}} & \text{for } 0 \leq E - qU \leq \Delta E, \\ 1 & \text{otherwise.} \end{cases} \quad (2.5)$$

Fig. 2.2 plots an example of the transmission function.

### 2.2.2 Energy Loss and Response Function

Electrons lose energy by scattering on the gas molecules in the source. This effect has to be taken into account to accurately describe which electrons pass the filter. The energy loss

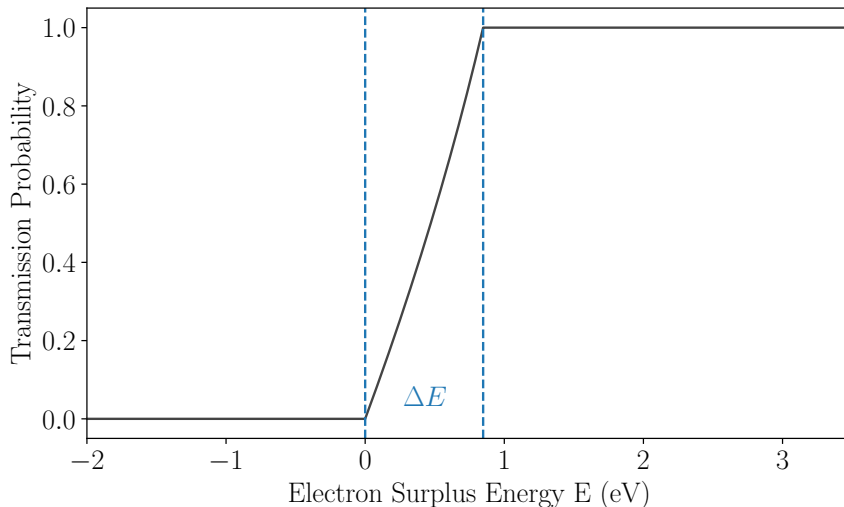


Figure 2.2: An example for the transmission function of a MAC-E Filter set at the retarding potential  $qU = 18500$  eV using the KATRIN design values. Additionally the energy resolution  $\Delta E = 0.93$  eV is shown.

function  $f(\epsilon)$  describes with which probability the electron loses the energy  $\epsilon$  [Ase+00]:

$$f(\epsilon) = \frac{1}{\sigma} \cdot \frac{d\sigma}{d\epsilon}, \quad (2.6)$$

where  $\sigma$  is the inelastic cross section.

The electron can scatter multiple times while traveling in the source. For  $n$ -fold scattering the transmission function is convolved with the energy loss function  $n$  times. The contribution from each scattering is weighed by the scattering probabilities  $P_n$ .

We can then express the response function as follows:

$$\begin{aligned} R(E, qU) &= P_0 \cdot T(E, qU) * \delta(\epsilon) + \\ &P_1 \cdot T(E, qU) * f(\epsilon) + \\ &P_2 \cdot T(E, qU) * f(\epsilon) * f(\epsilon) \dots \\ &= T(E, qU) * \sum_{i=0}^{n_{\max}} P_i f_i(\epsilon), \end{aligned} \quad (2.7)$$

where  $P_i$  and  $f_i(\epsilon)$  are the respective probabilities and energy loss functions for the  $i$ -th scattering.  $n_{\max}$  describes the maximum number of scattering we consider for the generation of our model. It is usually between 5 and 10, as the probabilities for higher scatterings become negligible. Fig. 2.3 plots the contribution from the energy loss and fig. 2.4 shows an example of the response function.

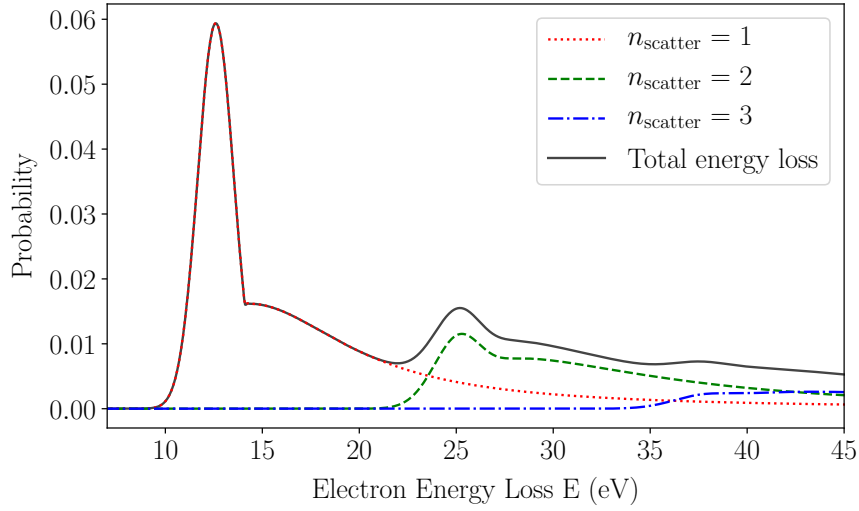


Figure 2.3: Energy loss contribution from the first four scatterings.

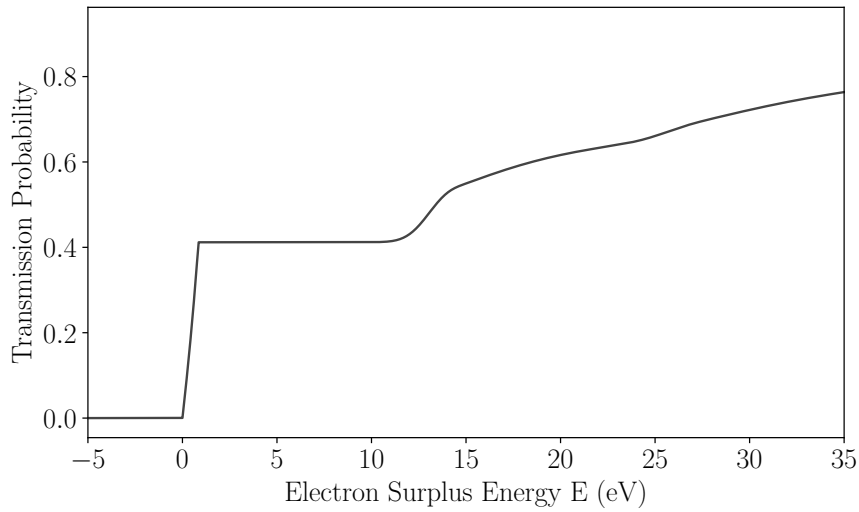


Figure 2.4: The response function for the KATRIN experiment with design values set at the retarding potential  $qU = 18500$  eV in the range of the first two electron scatterings.

### 2.2.3 Run Taking

**Measuring Time Distribution** The scanning procedure of a run can be expressed by the measuring time distribution (MTD). It describes how much time is spent measuring counts at which retarding potentials. The simplest MTD is the so-called flat MTD which measures the spectrum at equidistant retarding potentials for equal durations.

**Run Summary** The information about the experiment during one run is called *run summary*. It includes the experimental measurements, such as counts and measuring time, as well as the slow control parameters of the setup, provided by the monitoring facilities such as the Laser Raman system [Sch+13] or the forward beam monitor [Ell+17].

# Chapter 3

## Statistics

This chapter outlines the statistical methods used in this work. Core of the approach is the Bayesian school of analysis on which we also give a short introduction here.

### 3.1 Choice of Likelihood

The likelihood describes the conditional density of the data given the model expectation. Since we expect the electrons to arrive at a certain rate at the detector and the events are independent of each other, we choose the Poisson distribution as the probability distribution function describing our spectrum counts in the likelihood function for our analysis.

### 3.2 Bayesian School of Analysis

The essence of Bayesian statistics is to update a prior knowledge with acquired data to obtain posterior knowledge. This is implied in Bayes' theorem:

$$P(\theta|D) = \frac{P(D|\theta)P(\theta)}{\int P(D|\theta)P(\theta) d\theta}, \quad (3.1)$$

where  $\theta$  is the vector of parameters of a model and  $D$  is the data measured by an experiment.  $P(\theta|D)$  is the so-called posterior probability function that describes the probability distribution assigned to a set of parameters given a set of data.  $P(D|\theta)$  is the probability of a set of data given set of parameters, also known as the likelihood.

**Prior Probability Distribution**  $P(\theta)$  is the so-called prior probability distribution. It can describe any prior knowledge of the system, such as theoretical constraints, measurements of systematic parameters, or experimental results. In this case it would be called an informative prior. It is also possible to use a non-informative prior; the most commonly used is a constant distribution, also known as the flat prior.

**Posterior Probability Distribution** From eq. (3.1) we then obtain the posterior probability distribution by sampling the posterior space. This is the full result of the Bayesian analysis. We can then marginalize our parameters of interest, i.e. integrate over the nuisance parameters  $\nu$ :

$$P(\theta|D) = \int P(\theta, \nu|D) d\nu. \quad (3.2)$$

In other words, we sum over all possible nuisance parameter sets, weighted by their probability, to obtain the posterior distribution on our parameter of interest. We can then infer values and uncertainties of our parameters of interest directly from the marginal posterior distributions. We will favor the 95% credible intervals (CI) and the posterior mean, i.e. the mean values of the marginalized posterior distributions for each fit parameter. The *corner.py* package [For16] is used for visualization.

**Treatment of Systematic Uncertainties** In the Bayesian framework the treatment of systematic uncertainties is very straightforward. We can introduce a parameter that describes the systematic uncertainty and apply a prior characterizing its behavior, e.g. a Gaussian function with a mean and width corresponding to the expected values. When marginalizing for the physical parameters, the impact of the systematic parameters will manifest themselves in the posterior distributions.

**Bayes Factor** The role of the integral in the denominator is to normalize the posterior. It is also known as the *evidence*  $Z$ , or marginal likelihood. For the mere inference of parameters its calculation is not necessary, however it is practical for comparing models. Via the posterior odds  $O$ :

$$O = \frac{P(M_1|D)}{P(M_2|D)} = \frac{P(D|M_1)}{P(D|M_2)} \cdot \frac{P(M_1)}{P(M_2)}, \quad (3.3)$$

where  $P(M_1)$  and  $P(M_2)$  are the prior probabilities for model  $M_1$  and model  $M_2$  respectively. We then make model comparisons based on  $O$ . The prior odds  $\frac{P(M_1)}{P(M_2)}$  describe how much credence we lend to each model a priori. Often times we do not prefer any model; then the posterior odds reduce to the first ratio, called the Bayes Factor  $K$ :

$$K = \frac{P(D|M_1)}{P(D|M_2)} = \frac{\int P(D|\theta, M_1)P(\theta, M_1) d\theta}{\int P(D|\theta, M_2)P(\theta, M_2) d\theta} = \frac{Z_1}{Z_2} \quad (3.4)$$

We can use the evidence  $Z$  from different models to compare them to each other. Contrary to tests such as the Likelihood Ratio test this method does not just take the best fit into account, but the whole model exploration and naturally penalizes additional degrees of freedom. However it can be computationally difficult to calculate the marginal likelihood, as it involves a multidimensional integral. To solve the integral, many techniques exist. We tested the 'Numerical Lebesgue Algorithm' [Wei12] and a modified Harmonic

Mean approach [Raf+07]. The results mentioned in this work are computed with the former. We then use the scales provided by [Jef61][LW14] to translate the calculated Bayes factors into qualitative statements about the compared models.

### 3.3 Bayesian Analysis Toolkit

In this work, we use the Bayesian Analysis Toolkit (BAT), a software developed at the Max Planck Institute for Physics [CKK09]. It uses Monte Carlo Markov Chains (MCMC) with a Metropolis-Hastings algorithm to probe the provided likelihood space. Monte Carlo methods are of special interest in Bayesian analysis, as they excel in multiple dimensions and the marginalization of therein. The Metropolis-Hastings algorithm works as follows:

Given an initial set of parameters  $\theta_0$ ; for each iteration  $i$ :

1. Propose a new set of parameters  $\hat{\theta}$
2. Calculate the ratio between posterior probabilities for the proposed set of parameters and the set of parameters of the last iteration  $i - 1$ :  

$$C = P(\hat{\theta}|D)/P(\theta_{i-1}|D).$$
3. Generate a random number  $g$  according to the uniform distribution between  $[0,1]$
4. If  $g < C$  set  $\theta_i = \hat{\theta}$ , else  $\theta_i = \theta_{i-1}$

In other words, for every step a point gets proposed. We then calculate the value for the target function  $P(\theta|D)$  using this point. If this value is bigger than the previous one, the new point gets accepted. If it is smaller, it gets accepted with a certain probability according to the condition  $C$ ; otherwise it is rejected and the old one is kept. For each iteration we obtain a sample of coordinates in the parameter space. The condition  $C$  ensures that we explore the parameter space in a way that is, by the law of large numbers, proportional to the posterior distribution. The posterior probability in an interval is then proportional to the number of samples in this interval. Therefore if we want to visualize an approximation of the posterior, we have to bin the samples in a histogram.

The results of the Markov chain will be initially dependent on the first point. However given certain conditions and an infinite run time, it will perfectly replicate the target function  $P(\theta|D)$ . By comparing separate Markov chains, BAT can estimate when the difference is negligible i.e. the Markov chain has converged. The time for this to happen is also called *burn-in period*. We only consider the samples after that; the samples from the burn-in in period are discarded.

## Chapter 4

# Strategies for Handling the Structure of the Focal Plane Detector

The KATRIN Focal Plane Detector is segmented in 148 pixels. They are effectively independent detectors that count their own spectrum. Additionally, they also have their own systematic parameters: based on their position relative to the experimental setup, their magnetic and potential fields have to be corrected in the model. We then end up with effectively 148 spectra and models. In the following we discuss different methods to combine them.

### 4.1 Single-Pixel Fits

The easiest way is to analyze each pixel separately and end up with 148 posteriors. This allows for diagnostic options. Fit results, such as posterior means, can be displayed in a heat map using the geometry of the FPD to look for patterns.

To obtain a value that combines the results, it is possible to average the fitted parameters values from each pixel, e.g. by weights. However, this makes the assumption that the errors on the values are purely of statistical nature. This might not be applicable in most cases.

### 4.2 Uniform Fits

Another easy way is to omit the structure of the FPD. The detector can be treated as one single pixel where the registered counts and measuring times are added and slow control parameters of the pixels are averaged.

This option is suitable for producing fast results, as we only have to simulate one model. Additionally, we effectively reduce the statistical error, making it a good option if we have little data at hand. However, this adds a systematic error to our results. If the spectra differ systematically, e.g. are shifted with respect to each other, we introduce a smearing effect. This can, in the case of the neutrino mass measurement, lead to a negative shift in the observed neutrino mass [Sle15]. It should not be pursued for final analyses.

### 4.3 Multi-Pixel Fits

The method we deem the most correct is to regard the total likelihood of the detector as the product of pixel-dependent likelihood terms:

$$P_{\text{total}} = \prod_{i=1}^{n_{\text{Pixel}}} P_i(\theta, \nu_i | D_i). \quad (4.1)$$

The likelihood terms share a global parameter vector  $\theta$  while keeping their own pixel-dependent parameter  $\nu_k$  and a spectrum  $D_k$  that a pixel sees.

The first intuition would be to use that likelihood directly for the analysis. We call this the *global fit*. However, assuming there are at least two pixel-dependent parameters, signal strength and background in most cases, this sums up to a minimum of 296 free parameters.

The Metropolis-Hastings algorithm, which BAT is based on, is not equipped to handle a large number of dimensions. As the proposal function is entirely probabilistic, it is possible that the Markov chain 'gets lost' in low probability areas. This leads to the duration of the burn-in period greatly scaling with the number of parameters to the point, where the analysis is very impractical or even impossible. BAT-2 [Sch18] will be equipped with the Hamiltonian Monte Carlo algorithm which exploits gradient information, which is especially advantageous in high dimensional spaces (see section 7.1). Unfortunately it was not available to us at the time of this thesis. Alternative techniques have to be considered. We propose two methods to deal with this problem.

#### 4.3.1 Chaining

We recall Bayes' theorem:

$$P(\theta|D) \propto P(D|\theta) \cdot P(\theta). \quad (4.2)$$

In other words, we use prior information in combination with data to obtain posterior information.  $P(\theta)$  can describe any prior knowledge, such as the results of prior experimental results. As we can consider the pixels of the FPD to be independent counting experiments, we can use Bayes' theorem to combine the experimental results of the pixels:

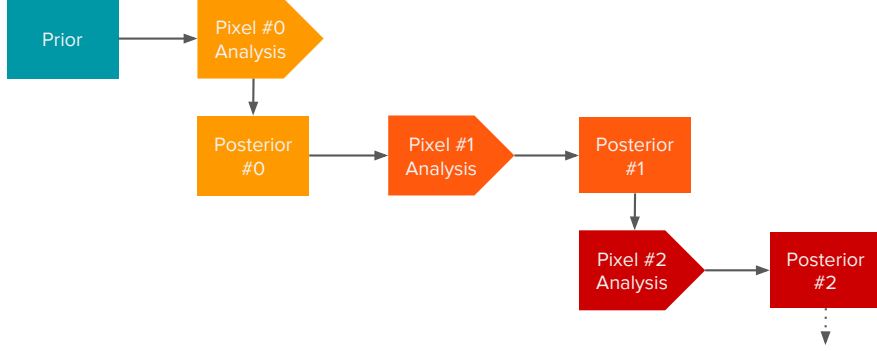


Figure 4.1: Schematic diagram of the chaining method. The posterior distribution of an analysis is iteratively used as the prior distribution of the next until all pixels are analyzed.

$$\begin{aligned}
 P_1(\theta|D_1) &\propto P_1(D_1|\theta) \cdot P_0(\theta|D_0) \\
 &\propto P_1(D_1|\theta) \cdot P_0(D_0|\theta) \cdot P(\theta).
 \end{aligned}
 \tag{4.3}$$

To analyze the next pixel, we can simply use the last obtained posterior as the prior for that analysis again. We can keep doing that until we have analyzed all pixels. We then obtain:

$$\begin{aligned}
 P_{N-1}(\theta|D_N) &\propto P_{N-1}(D_{N-1}|\theta) \cdot P_{N-2}(D_{N-2}|\theta) \cdot \dots \cdot P_0(D_0|\theta) \cdot P(\theta) \\
 &\propto \prod_{i=0}^{N-1} P_i(D_i|\theta)P(\theta),
 \end{aligned}
 \tag{4.4}$$

where  $N$  is the number of pixels we analyze. I.e. we use the posterior of one pixel as the prior information for the next, and so on. The product of likelihoods is equal in form to eq. (4.1). This proves that this serial knowledge updating is equivalent to evaluating the product of likelihoods.

Fig. 4.1 shows a schematic overview of the method. This is a very elegant way of using the Bayesian framework to combine our pixel results. The method unfortunately does not come without caveats: We have to bin our MCMC samples from our posterior to be able to use it as a prior. Due to the finite bin width we will therefore lose resolution in our posterior.

### 4.3.2 Posterior Product

We are also interested in a fast way to obtain parameter estimates for our model, e.g. for quick comparisons of our data and model. Since we have 148 detectors with separate models and data, we want to parallelize their analyses and combine them at the end.

The posterior we want to obtain is:

$$P_{\text{total}}(\theta|D) \propto P_{\text{total}}(D|\theta) \cdot P(\theta). \quad (4.5)$$

$P_{\text{total}}(\theta|D)$  refers to eq. 4.1. In many cases we can express our prior in the following manner:

$$P(\theta) = \prod_{i=1}^{n_{\text{Pixel}}} P_i(\theta). \quad (4.6)$$

Combine eq. 4.1 with eq. 4.6 and we receive:

$$\begin{aligned} P_{\text{total}}(\theta|D) &\propto \prod_{i=1}^{n_{\text{Pixel}}} P_i(\theta|D_i) \cdot \prod_{i=0}^{n_{\text{Pixel}}} P_i(\theta) \\ &\propto \prod_{i=1}^{n_{\text{Pixel}}} P_i(\theta|D_i) \cdot P_i(\theta). \end{aligned} \quad (4.7)$$

This implies that, under the circumstance that the likelihoods and priors are independent of other pixels, we can express the global posterior as the product of all individual posteriors. Again, a caveat is that we have to bin our posterior samples. Additionally, the priors are limited to individual pixel basis. However, this method is highly parallelizable, especially when using a computing cluster. In this work we used the facilities of the *National Energy Research Scientific Computing Center* (NERSC). Each pixel analysis can be handled independently; afterwards the posteriors can be combined. One can see this as a 'Bayesian Single-Pixel Fit'. Fig. 4.2 shows the procedure of this approach.

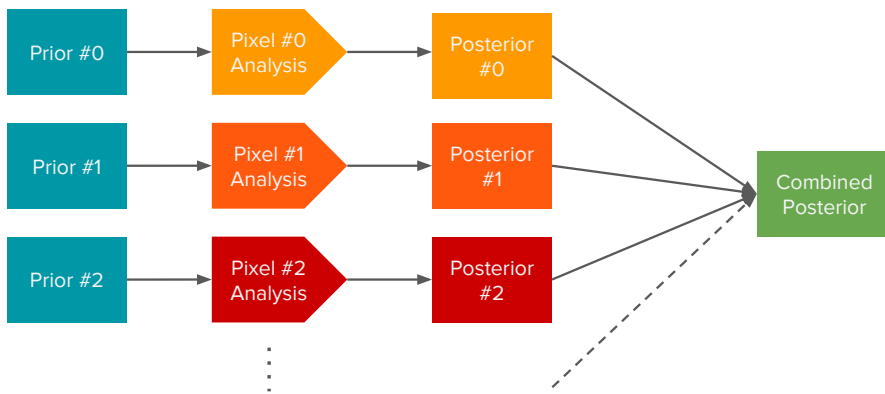


Figure 4.2: Schematic diagram of the posterior product method. Each pixel is analyzed separately in parallel; the binned posterior distributions are combined in end.

## Chapter 5

# The Gaseous $^{83\text{m}}\text{Kr}$ Source in the KATRIN Experiment

In summer 2017, in the phase leading up to the tritium measurements, we introduced a gaseous  $^{83\text{m}}\text{Kr}$  source in the KATRIN experiment. The gaseous krypton source allows us to test the complete KATRIN setup as it will be used for the tritium phase.  $^{83\text{m}}\text{Kr}$  emits monoenergetic conversion electrons at multiple energies, making it optimal for calibration purposes. This body of work focuses on the  $L_3$ -32 line. The goal of the analysis is to show how the BAT in combination with our models can be used to analyze the integral spectra, examine impact from systematic uncertainties, explore how different parameters correlate with each other, inquire information about our experimental setup, and test pixel combination methods.

### 5.1 Decay and Line Model

In the following we show the theoretical decay and spectral lines of  $^{83\text{m}}\text{Kr}$  and describe our modelling thereof.

#### 5.1.1 Decay

$^{83\text{m}}\text{Kr}$  has a half-life of 1.8 hours and is produced in the decay of  $^{83\text{m}}\text{Rb}$  [McC15][Vén+18]. Fig. 5.1 shows the decay scheme for this process.

It decays from its isomeric state while assuming an intermediate state in the process, with energy level differences of 32.2 keV and 9.4 keV respectively. This energy can be emitted in the form of conversion electrons, which are quasi-monoenergetic. They are therefore highly useful for the calibration of experiments detecting electrons, such as the KATRIN experiment. While there are different lines in the  $^{83\text{m}}\text{Kr}$  decay that can be used for different purposes, we will focus on the  $L_3$ -32 line, corresponding to an expected line position  $E_{\text{pos}} = 30472.2$  eV and width  $\Gamma = 1.19$  eV. Reason for this is the high

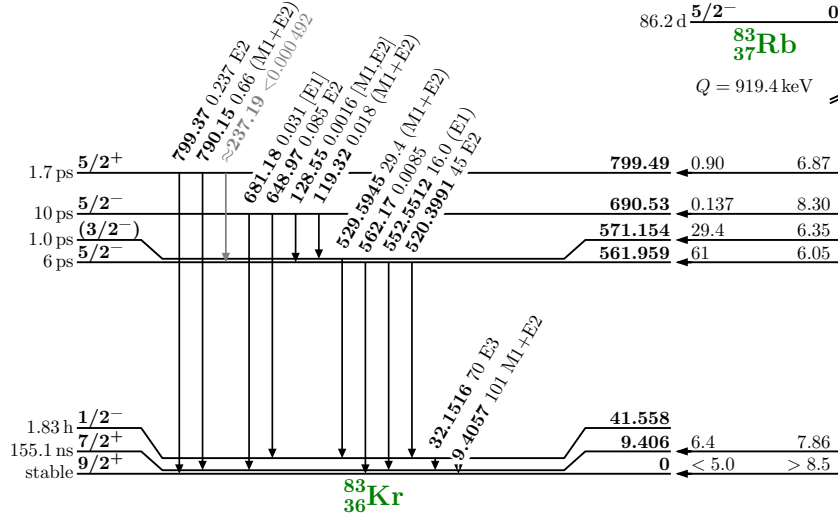


Figure 5.1: Decay scheme of  $^{83\text{m}}\text{Rb}$  into  $^{83\text{m}}\text{Kr}$ . This figure is from [Sle15], based on [McC15].

intensity per decay of 37.8% as well as its line width similar in magnitude to the KATRIN spectrometer energy resolution.

### 5.1.2 Differential Spectrum

We use a Lorentzian function to describe the differential shape of the line:

$$L(E, A, E_{\text{pos}}, \Gamma) = \frac{A}{\pi} \frac{\Gamma/2}{(E - E_{\text{pos}})^2 + \Gamma^2/4}. \quad (5.1)$$

$E_{\text{pos}}$  and  $\Gamma$  describe the line position and line width (full width at half maximum) respectively;  $A$  describes the normalization factor. Fig. 5.2 plots an example spectrum.

### 5.1.3 Thermal Doppler Effect

Due to the non-zero temperature of the gas source, the shape is broadened by a thermal Doppler effect. This is accounted for by convolving the Lorentzian function with a Gaussian function. This Gaussian is centered around zero and has a width  $\sigma = \sqrt{2EkT\gamma m/M}$ , where  $T$  is the gas temperature,  $k$  is the Boltzmann constant,  $m$  is the electron mass, and  $M$  is the mass of  $^{83\text{m}}\text{Kr}$ . In this case the temperature  $T$  is set to 100 K to prevent freeze-out on the beam tube walls. The mean of the Gaussian describes the flow of the gas, which we here assume to be negligible. The resulting function is also known as the Voigt function  $V$ .

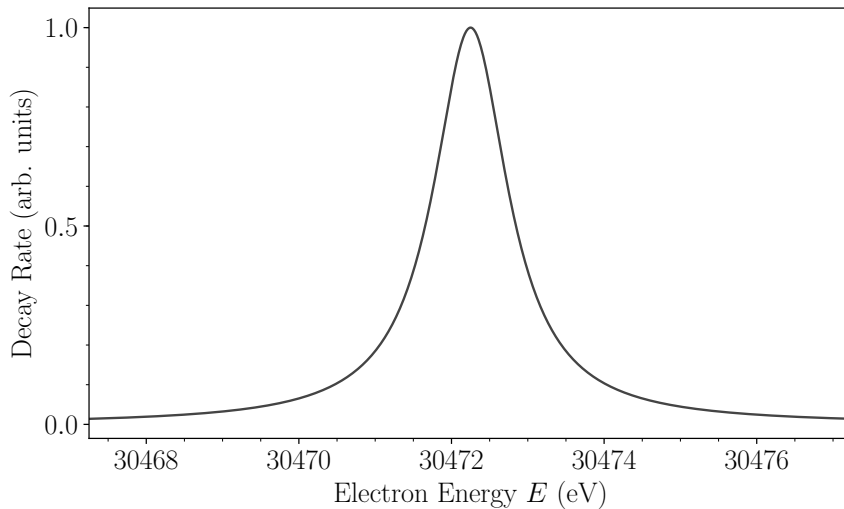


Figure 5.2: Lorentzian function describing the differential decay rate of the monoenergetic  $^{83\text{m}}\text{Kr}$  L<sub>3</sub>-32 line.

#### 5.1.4 Integrated Spectrum

During the krypton measurements the gas density was low enough so that energy loss by electron scattering was negligible. This reduces the response function to the transmission function, Equation (2.5). The integrated spectrum  $I$  can then be described by:

$$I(qU, A, E_{\text{pos}}, \Gamma) = \int_{-\infty}^{\infty} V(E, A, E_{\text{pos}}, \Gamma) T(E, qU) dE. \quad (5.2)$$

Fig. 5.3 shows an example for the integral and differential spectrum. As the MAC-E filter works as an integrating filter, electrons from energetically higher lines can pass through the spectrometer to the FPD. For our analysis, we expect their rate constant in our small analysis window. We therefore add a constant term  $C$  to account for this offset.

The model is then as follows:

$$M(qU, E_{\text{pos}}, \Gamma, A, C) = I(qU, E, \Gamma, A) + C. \quad (5.3)$$

Our parameters of interest in this case are the line position  $E_{\text{pos}}$  and the line width  $\Gamma$ , while the normalization  $A$  and the constant offset  $C$  are nuisance parameters. The software used for this analysis is a combination of the *Fitness Studio*, a software framework for fitting models to data by Martin Slezák [SK18], and the BAT.

#### 5.1.5 Likelihood Function

The likelihood function we use is then:

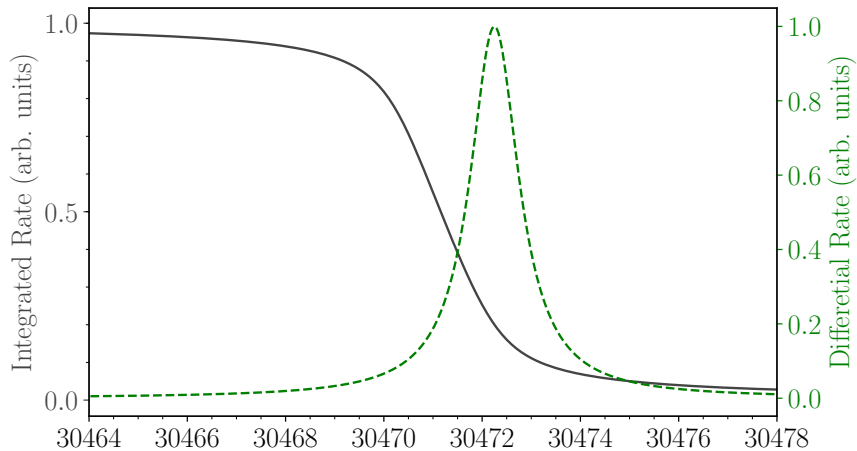


Figure 5.3: Integrated rate of the  $^{83\text{m}}\text{Kr}$  L<sub>3</sub>-32 line superimposed with the corresponding differential rate.

$$P(D, E_{\text{pos}}, \Gamma, A, C) = \prod_i \mathcal{P}[D(qU_i); M(qU_i, E_{\text{pos}}, \Gamma, A, C)], \quad (5.4)$$

where  $D(qU_i)$  is the number of counts measured at the retarding potential  $qU_i$  and  $\mathcal{P}(k; \lambda)$  is the Poisson probability for measured counts  $k$  given expected counts  $\lambda$ .

## 5.2 Analysis of the L<sub>3</sub>-32 Line

With the analysis of the L<sub>3</sub>-32 line of  $^{83\text{m}}\text{Kr}$  we want to show the usability of BAT. First, we present statistical only analysis, then we discuss the systematic uncertainties during the measurement and how they are handled. Additionally, we test the pixel combination techniques. We also show an estimation of the relative energy resolution of the KATRIN experiment. Table A.1 shows the settings used in this analysis.

### 5.2.1 Choice of Priors

We choose non-informative priors for this analysis. For both our physical parameters the line position  $E_{\text{pos}}$  and the line width  $\Gamma$ , as well as our nuisance parameters the amplitude  $A$  and the constant offset  $C$ , we use flat priors and restrict them to be positive.

### 5.2.2 Uniform-Fits

We start by examining the uniform fit. Fig. 5.4 shows the posterior distributions for  $E_{\text{pos}}$  and  $\Gamma$ . For the mean of the posterior we obtain 95% credible intervals for  $E_{\text{pos}} =$

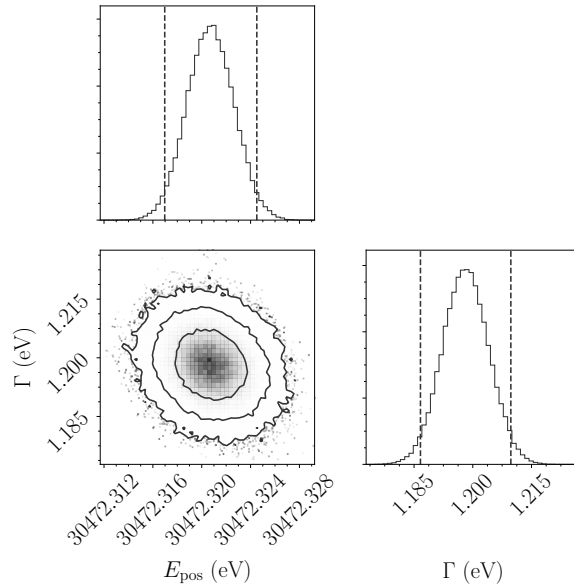


Figure 5.4: Marginalized posterior distributions for  $E_{\text{pos}}$  and  $\Gamma$  from a uniform fit. The contours show the 68%, 95% and 99.7% credible intervals. The dotted lines indicate the 95% credible intervals.

[30472.317, 30472.325] eV and  $\Gamma = [1.187, 1.210]$  eV. Fig. 5.5 shows the recorded spectrum as well as a model prediction using the obtained results.

### 5.2.3 Single-Pixel Fits

Next, we perform a single-pixel fit. Fig. 5.6 shows the marginalized posterior distributions and fig. 5.7 plots a fit for the innermost pixel. To inspect for pixel-dependent patterns, we plot the distribution of fit values across the FPD in fig. 5.8.

A dipole structure is visible in the heat map of the line position  $E_{\text{pos}}$ ; i.e. the inferred line position of the pixels on the right side seem to be shifted towards higher values compared to left side. There does not seem to be a pattern in the line width  $\Gamma$ , or at least it is not as extreme. At the moment we attribute this effect to a misalignment of the FPD [Cho18]. We will further investigate this in future measurements. In any case, we can conclude that we should not continue using the uniform fits here, as it introduces a systematic error by smearing the spectra. Since the number of events for the krypton measurements is rather high, we will for now analyze the innermost pixel for the sake of simplicity.

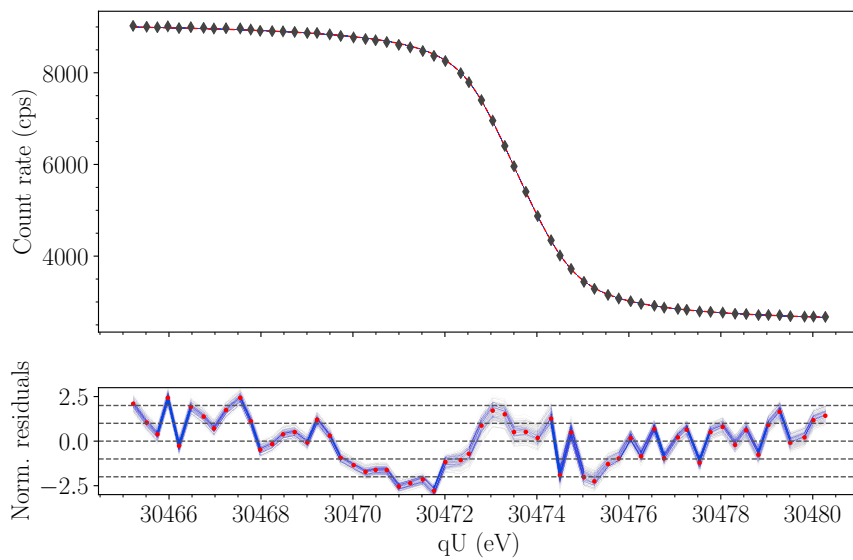


Figure 5.5: Spectrum of the measured count rate and model predictions from the posterior distribution for a uniform fit. The blue lines represent model predictions drawn from the posterior distribution: We take 2000 MCMC samples, corresponding to multi-dimensional parameter vectors, with which we calculate a model prediction for the spectrum; these predictions can then be visualized as shown above. We use this method in all subsequent spectral plots. The red items represent information from the posterior mean.

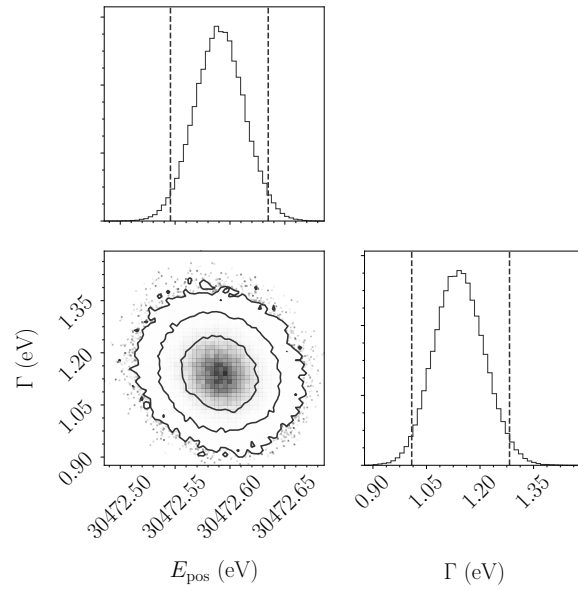


Figure 5.6: Marginalized posterior distributions for  $E_{\text{pos}}$  and  $\Gamma$  from a fit for the innermost pixel. The contours show the 68%, 95% and 99.7% credible intervals. The dotted lines indicate the 95% credible region.

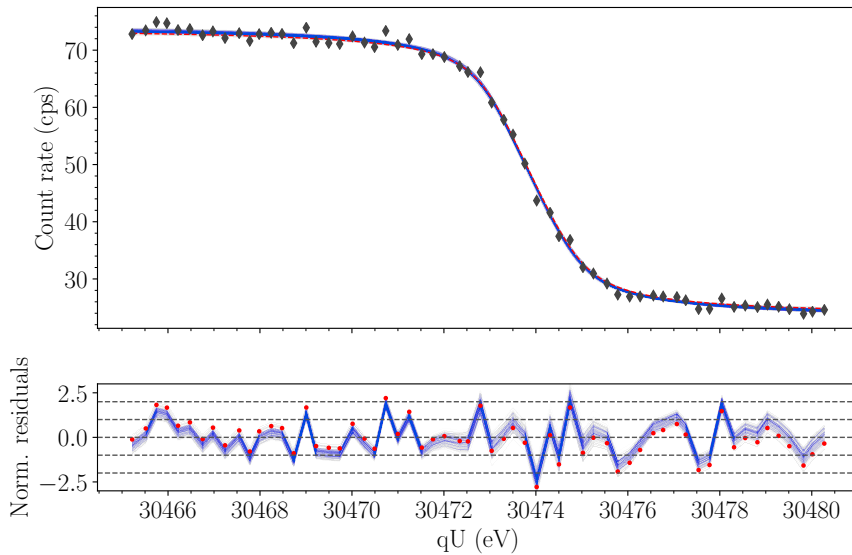


Figure 5.7: Spectrum of the measured count rate and model predictions from the posterior distribution fit using the innermost pixel. The blue lines represent model predictions drawn from the posterior distribution. The red items represent information from the posterior mean.

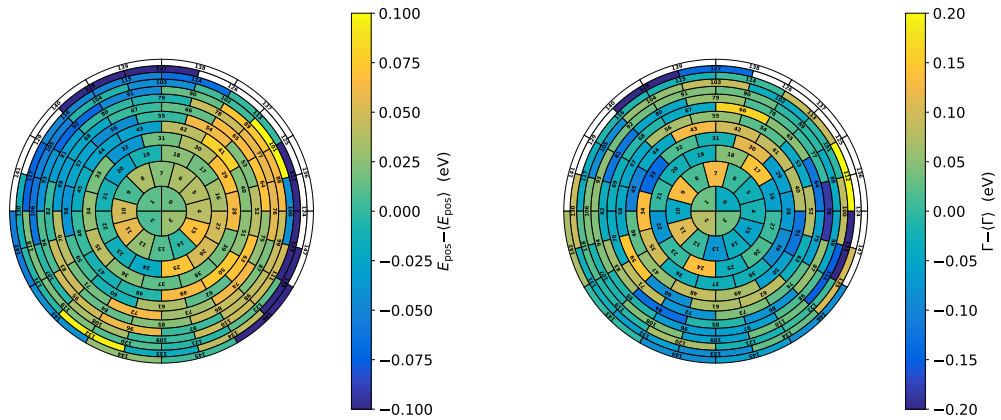


Figure 5.8: Heat maps of the line position  $E_{\text{pos}}$  (left) and line width  $\Gamma$  (right) relative to their respective means for a single-pixel fit. The excluded pixels are not filled. A dipole structure is visible in the heat map of  $E_{\text{pos}}$ .

#### 5.2.4 Multi-Pixel Fits

We now want to test our pixel combination methods. We choose the first 40 pixels, corresponding to the 4 innermost pixels and the first 3 rings. For the chaining method, we start with a flat prior on  $E_{\text{pos}}$  and  $\Gamma$  and use the marginalized posterior distribution for  $E_{\text{pos}}$  and  $\Gamma$  of one analysis as the prior for the subsequent one. For the posterior product method we analyze each pixel separately and combine the results in the end by multiplying the marginalized posterior distributions. Fig. 5.9 shows a comparison of the marginalized posterior distributions for this analysis.

We can see that the marginalized posterior distributions generally agree in their shape and range up to a minuscule shift. However the posterior product has an uneven behaviour. The posterior distributions of the individual pixels are shifted in position (see fig. A.2). Therefore the common range is rather small. To accommodate for this, a finer binning is necessary. However, this increases the uncertainty on the bin content, due to the finite amount of samples, leading to an uneven behavior of the posterior shape. This propagates into the posterior product. A solution to this would be to have a longer run time for the MCMC to produce more samples.

Nevertheless we can produce credible intervals. The results are shown in table 5.1. We can see that the credible intervals match very well, up to a small shift, as expected from the visual inspection of the marginalized posteriors.

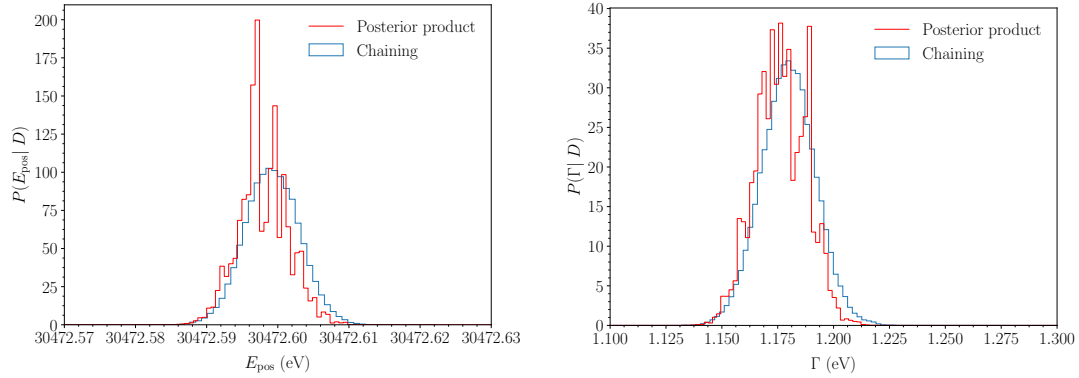


Figure 5.9: Comparison of the the marginalized posterior distributions for  $E_{\text{pos}}$  (left) and  $\Gamma$  (right) using different multi-pixel fit strategies. The number of samples in this analysis was not enough to accommodate for the fine binning necessary, leading to the uneven behaviour of the posterior product.

Table 5.1: 95% credible intervals for the line position  $E_{\text{pos}}$  and the line width  $\Gamma$  for different multi-pixel methods.

Method	Line position $E_{\text{pos}}$	Line width $\Gamma$
Chaining	[30472.592, 30472.607]	[1.156, 1.204]
Posterior product	[30472.591, 30472.606]	[1.152, 1.198]

### 5.3 Discussion of Systematic Uncertainties

The main source of systematic uncertainty we experience in the krypton measurements is the so-called high voltage ripple. Due to the 50 Hz frequency of the grid power's alternating current, there is a small oscillating change of the retarding voltage applied to the main spectrometer. This effect is exclusive to the krypton measurements analyzed in this thesis. In the final measurement a post-regulation system will be applied. An electron that enters the main spectrometer experiences a retarding potential, and by extension a transmission function, that is slightly modified by the high voltage ripple. As the electrons are fast compared to the change of the high voltage we can postulate:

$$T^*(E, qU) = \frac{1}{\pi} \int_{-\pi/2}^{\pi/2} T(E, qU + qA_{\text{HV}} \cdot \sin \phi) d\phi, \quad (5.5)$$

where  $A_{\text{HV}}$  is the amplitude of the high voltage ripple, or the magnitude of the maximum change of voltage from the set retarding potential  $qU$ . Pragmatically,  $A_{\text{HV}}$  leads to an additional width in the integrated spectrum. This makes it difficult to estimate the extent of  $A_{\text{HV}}$  by fitting the data: The observed width  $\Gamma_{\text{obs}}$  is a combination of the decay width  $\Gamma_{\text{Kr}}$  and the width caused by the inseparable high voltage ripple  $\Gamma_{\text{HV}}$ . This means that the contribution to the line width by one effect can be absorbed by the other when fitting. The spectrometer resolution also contributes a width, however it is here fixed by the magnetic fields.

We can confirm this in practice: We set a positive definite flat prior on  $\Gamma_{\text{HV}}$  and perform a fit for the innermost pixel. Figure 5.10 shows the posterior distributions for  $\Gamma$  and  $A_{\text{HV}}$ . From its shape we cannot infer a value on  $A_{\text{HV}}$ , however we can set an upper limit of 673.7 mV at a 95% credible interval. The two-dimensional marginalized posterior distribution of  $\Gamma$  and  $A_{\text{HV}}$  shows also an anti-correlation, as we expected.

Measurements estimate  $A_{\text{HV}}$  to 208 mV with a relative error of 20% [Are+18]. We will use this value to evaluate its impact on the measurements by setting a Gaussian prior with these values and performing a fit for the innermost pixel. Fig. 5.11 shows a knowledge update for the HV ripple amplitude  $A_{\text{HV}}$  and a comparison with the marginalized posterior distribution using a flat prior. From the knowledge update plot we can infer the contribution from the data gets dominated by the influence of the informative prior, as the shape of the marginalized posterior lines up almost exactly with the prior.

Fig. 5.12 shows a comparison of the marginalized posterior distributions for the line position  $E_{\text{pos}}$  and the line width  $\Gamma$  for different priors. We see the impact of the different priors mostly with  $\Gamma$ , as we expected: The higher the amplitude of the HV ripple, the higher is its contributed width;  $A_{\text{HV}}$  and  $\Gamma$  are strongly anti-correlated. The line width  $\Gamma$  can then decrease to compensate and keep the overall observed width constant. Therefore we see a shift of the posterior in  $\Gamma$  when we set  $A_{\text{HV}}$  to non-zero values. Additionally the posterior in  $\Gamma$  widens if the HV ripple amplitude can also assume a large range of values.

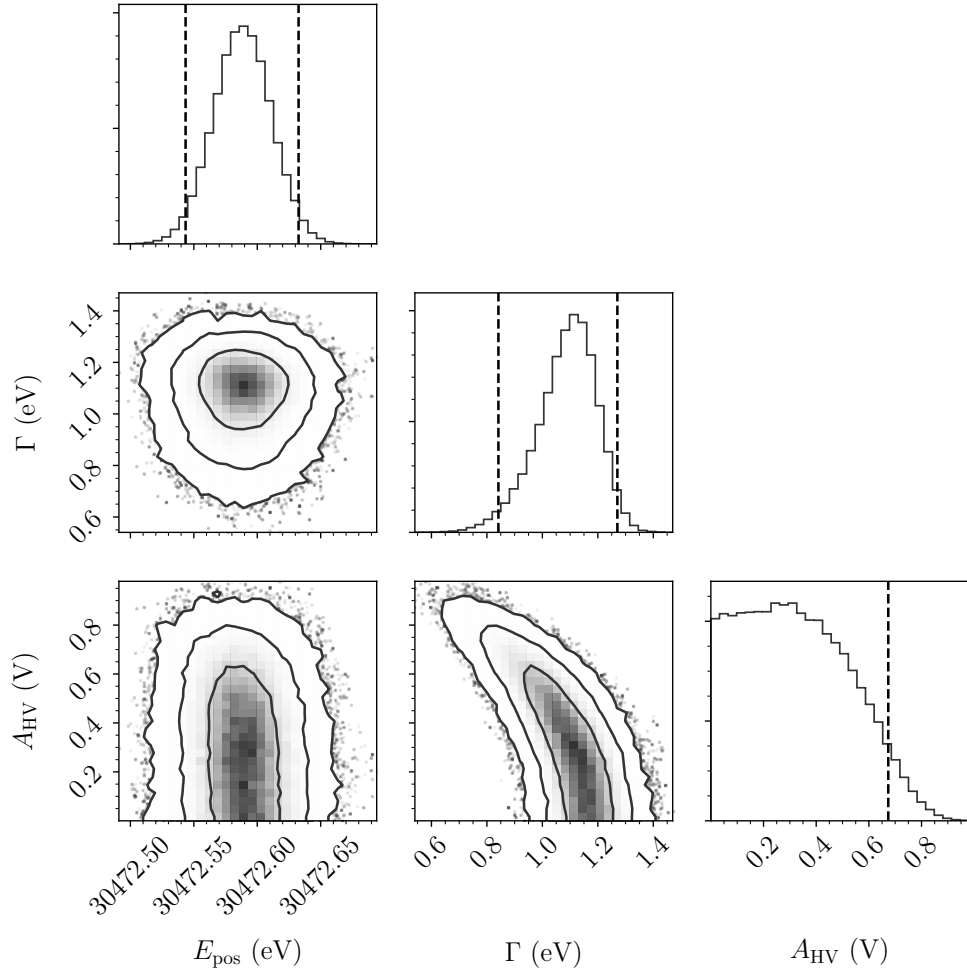


Figure 5.10: Marginalized posterior distributions of the line position  $E_{\text{pos}}$ , line width  $\Gamma$ , and HV ripple amplitude  $A_{\text{HV}}$  for a fit using the innermost pixel. From the experimental data we obtain an upper limit of  $A_{\text{HV}} < 673.7$  mV at a 95% credible level.

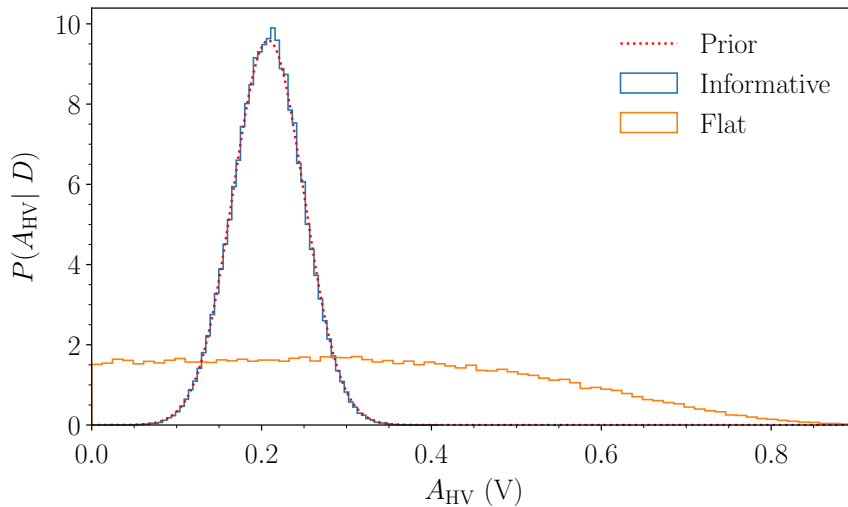


Figure 5.11: Knowledge update for the HV ripple amplitude with an informative prior using prior measurements and comparison with a marginalized posterior for a flat prior for the innermost pixel.

Since the line position  $E_{\text{pos}}$  is not strongly correlated to the observed line width, the effect of different priors on the HV ripple amplitude  $A_{\text{HV}}$  is minuscule.

## 5.4 Estimating the Energy Resolution of the KATRIN Experiment

The total observed width is a combination of the natural line width of the  $L_3$ -32 line, the contribution from the HV ripple, and the spectrometer resolution of the KATRIN experiment. With that knowledge, we can estimate the latter. We recall the relation for a MAC-E filter:

$$\frac{\Delta E}{E} = \frac{B_A}{B_{\text{max}}}. \quad (5.6)$$

The form showed here is the non-relativistic approximation. By fitting the ratio of the magnetic fields we can make statements about the relative energy resolution. For this analysis we use more informative priors; additionally to the prior on the HV ripple amplitude  $A_{\text{HV}}$  we now also set a prior on the line width  $\Gamma$ , as the resolution will correlate strongly with any contribution to the observed width. The line width  $\Gamma$  of the  $L_3$ -32 line is not known very precisely, so we will set a conservative estimate of 20% relative error for our Gaussian prior. The spectrometer resolution can vary freely under a flat prior.

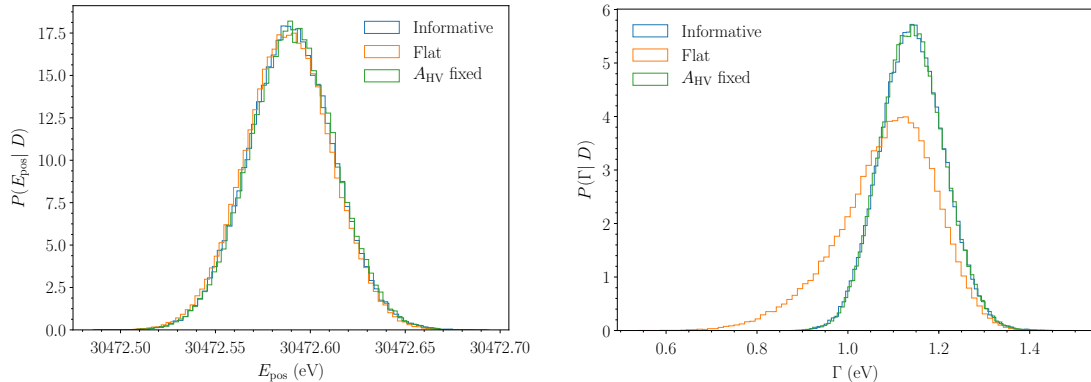


Figure 5.12: Comparison of marginalized posterior distributions of the line position  $E_{\text{pos}}$  (left) and line width  $\Gamma$  (right) using different priors for a fit of the innermost pixel. The ”informative” prior is a Gaussian on the HV ripple amplitude with a 20% relative width centered around 208 mV, corresponding to the results of prior measurements. The posterior for the line width  $\Gamma$  widens with a flat prior on  $A_{\text{HV}}$  due to the high correlation with  $A_{\text{HV}}$ .  $E_{\text{pos}}$  is not strongly correlated with  $A_{\text{HV}}$  and is thus barely affected by different priors on  $A_{\text{HV}}$ .

Fig. 5.13 shows the marginalized posterior distributions for this analysis. As we expected, the line width  $\Gamma$  is strongly correlated with the energy resolution. The two-dimensional marginalized posterior for  $\Delta E/E$  and the HV ripple amplitude  $A_{\text{HV}}$  seems to not show a strong correlation; this is due to the constraint from the prior on  $A_{\text{HV}}$ . A rather unexpected correlation can be seen between  $\Delta E/E$  and the line position  $E_{\text{pos}}$ . A widening of the energy resolution also leads to a widening of the transmission function, which will shift the center of the slope of the transmission function. This effectively leads to higher observed energies.

The 95% credible intervals for the relative energy resolution is  $\frac{\Delta E}{E} = [3.27, 7.54] \cdot 10^{-5}$ , corresponding to  $[0.61, 1.40]$  eV at 18.6 keV. This is a highly satisfying result, as it covers the expected value of 1.20 eV. From this we can deduce that the KATRIN experiment fulfills the requirements for the MAC-E filter principle.

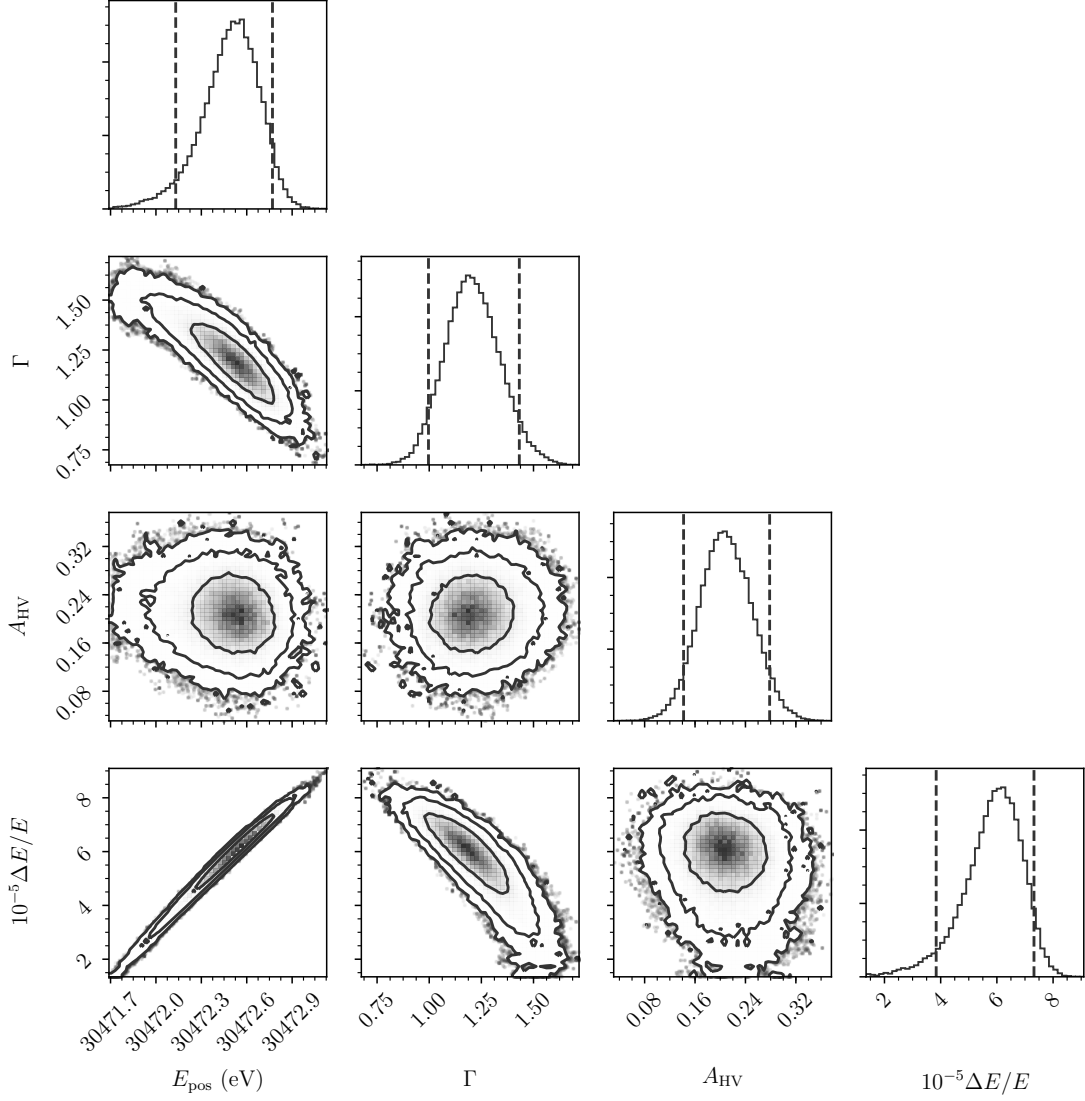


Figure 5.13: Marginalized posterior distributions for the evaluation of the relative energy resolution for a fit using the innermost pixel. The energy resolution strongly correlates with the line width  $\Gamma$ ; the correlation with the HV ripple amplitude  $A_{\text{HV}}$  is suppressed by the constraint of its prior. The line position  $E_{\text{pos}}$  is strongly correlated due to the correlation of the energy resolution with the slope of the transmission function, leading to a shift in the mean of detected energies. We obtain a 95% CI of  $\Delta E/E = [3.27, 7.54] \cdot 10^{-5}$ .

# Chapter 6

## First Tritium Data

In June 2018 we performed the *First Tritium* measurements. The purpose of this phase was to test the KATRIN experimental setup with tritium for the first time, to test the stability of the source parameters, and also to test our analysis tools with actual tritium data.

In this section we will first describe our modelling of the tritium spectrum. Then we will show our analysis strategies, examining both single- and multi-pixel fit analyses before we discuss the systematic uncertainties we identified and how we handle them.

### 6.1 Description of the Tritium Spectrum

The differential decay rate of a tritium spectrum is derived from Fermi's Golden Rule [OW08]:

$$\frac{d\Gamma}{dE} = C \cdot F(Z, E) p(E + m_e) E_\nu \sum_i |U_{ei}|^2 \sqrt{E_\nu^2 - m_i^2} \Theta(E_\nu - m_i). \quad (6.1)$$

With natural units so that  $c = 1$  and  $\hbar = 1$ .  $C = \frac{G_F^2}{2\pi^3} \cos^2 \theta_C |M|^2$ , where  $G_F$  is the Fermi constant,  $\theta_C$  is the Cabibbo angle, and  $M$  is the nuclear matrix element. The Fermi function  $F(Z, E)$  takes the Coulomb interaction between the emitted electron and the daughter nucleus with the charge  $Z$  into account.  $p$ ,  $E$ , and  $m_e$  are the momentum, energy, and mass of the electron, respectively.

To account for the different neutrino flavors it is necessary to sum over the mass eigenstates  $m_i$ . The fraction of contribution of each term is determined by the absolute square of the neutrino mass mixing elements  $U_{ei}$ . Due to the resolution of KATRIN, we can simplify by considering the effective electron neutrino mass  $m_\nu^2 = \sum_i |U_{ei}|^2 m_i^2$  [FS03]. As the logarithm of the likelihood is parabolic in  $m_\nu^2$ , not  $m_\nu$ , we can say that our observable is not the effective electron neutrino mass but the effective electron neutrino mass squared.

$E_\nu$  describes the neutrino energy  $E_\nu = E_0 - E$ , where  $E_0$  is the so-called endpoint energy of the tritium spectrum, the maximum energy an electron can assume with  $m_\nu = 0$ . The Heaviside function  $\Theta$  ensures energy conservation.

Molecular tritium decays as follows:



The resulting daughter molecule can then end up in an excited rotational, vibrational, or electronic state. To accommodate for this, the formula for the neutrino energy  $E_\nu$  can be amended:

$$E_\nu \rightarrow \tilde{E}_\nu = E_0 - V_f - E. \quad (6.3)$$

$V_f$  is the energy associated with the final state  $f$ . Equation (6.1) then has to be expanded with the summation over the final states  $f$  and their probabilities  $P_f$  to decay into:

$$D(m_\nu^2, E_0, E) = C \cdot F(Z, E) p(E + m_e) \sum_f P_f \tilde{E}_\nu \sqrt{\tilde{E}_\nu^2 - m_\nu^2} \Theta(\tilde{E}_\nu - m_\nu). \quad (6.4)$$

The final state distributions, that indicate which final states  $f$  can be assumed with probability  $P_f$  and energy  $V_f$ , are known from theoretical calculations. Their inclusion and accuracy is of utmost importance for the precise measurement of the neutrino mass. In this work, we use the calculations from [Dos+06] [DT08]. Fig. 6.1 shows the distribution of the final states used in this analysis.

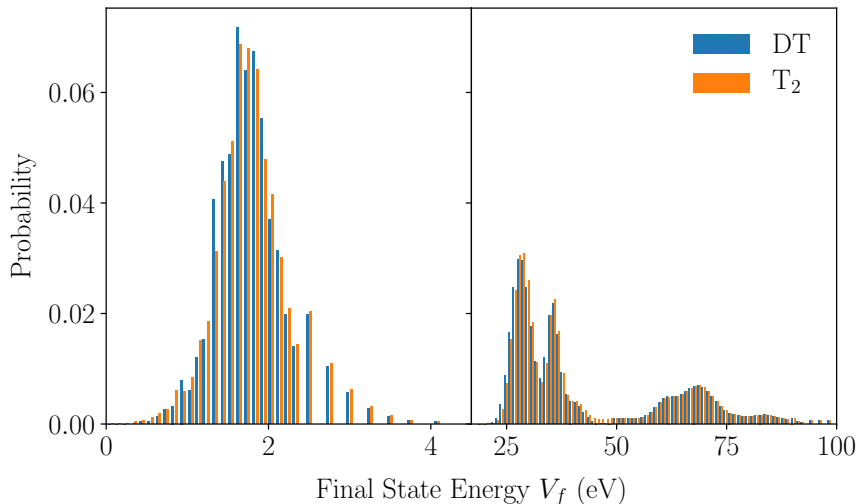


Figure 6.1: Binned final state distributions used in this work for different isotopologues. The shift of the bins between the models are purely for visual enhancement.

Equation (6.4) is the form we use in this work to model the tritium spectrum. If we integrate it with the Response Function eq. (2.7) we obtain the Integrated Spectrum  $I$ :

$$I(qU, m_\nu^2, E_0) = \int_{qU_{\min}}^{E_0} R(qU, E) \cdot D(m_\nu^2, E_0, E) dE. \quad (6.5)$$

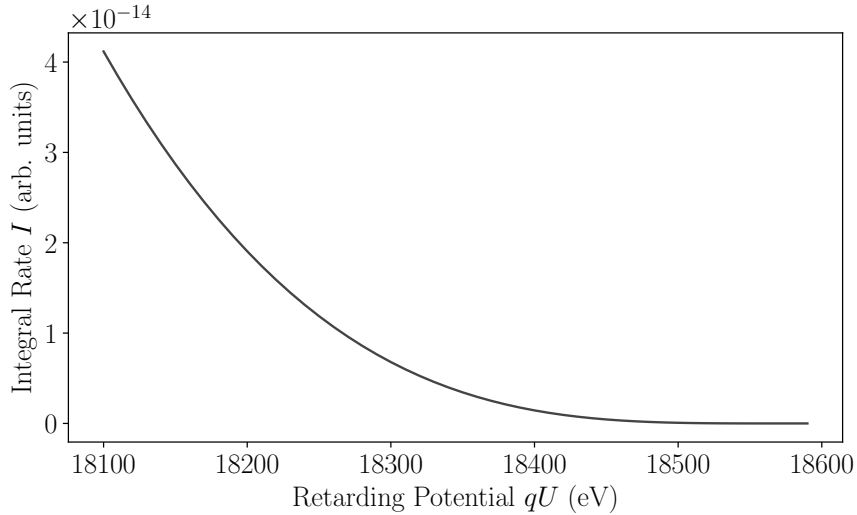


Figure 6.2: Example of the integrated spectrum with  $m_\nu^2 = 0$  and  $E_0 = 18575$  eV for KATRIN design values.

Fig. 6.2 plots an example for an integrated spectrum. Due to solid states effect, the observed electron energy is shifted by the difference of the work functions  $\Phi$  of the source and the spectrometer. This effectively leads to a shift of from the true values  $E$  the observed energies  $qU$ :

$$E = qU - (\Phi_{\text{Source}} - \Phi_{\text{Spectrometer}}). \quad (6.6)$$

A constant shift of the observed energies will not influence our measurement of the neutrino mass [Sle15]. However it will influence values of the endpoint  $E_0$ . At the moment we do not have a precise handle on the magnitude of this shift. For now we assume a conservative estimate of  $\pm 1$  eV. We therefore denote our observed endpoint as the effective endpoint  $E_0^{\text{eff}}$ .

Additionally we expand the model by multiplying the Integrated Spectrum with a normalization constant  $A$  as well as adding a constant offset  $C$  as a background model:

$$M(qU, m_\nu^2, E_0^{\text{eff}}, A, C) = A \cdot I(qU, m_\nu^2, E_0^{\text{eff}}) + C. \quad (6.7)$$

In the neutrino mass analysis the parameter of interest is obviously  $m_\nu^2$ . However, in our First Tritium measurement phase we do not attempt to measure the neutrino mass,

as the statistical uncertainties close to the endpoint are too large. Therefore, almost no neutrino mass information is contained in our first data. This makes  $m_\nu^2$ , in this analysis, along with  $A$  and  $C$  a nuisance parameter. We use a combination of the *Fitrium* software by Christian Karl [Kar18], based on the *Fitness Studio* framework by Martin Slezák, and BAT.

## 6.2 Likelihood Function

We use the following likelihood function for our analysis:

$$P(D|E_0^{\text{eff}}, m_\nu^2, A, C) = \prod_i \mathcal{P}_i(D(qU_i); M(qU_i, E_0^{\text{eff}}, m_\nu^2, A, C)). \quad (6.8)$$

Where  $D(qU_i)$  are the counts measured at the retarding potential  $qU_i$  and  $\mathcal{P}(k; \lambda)$  is the Poisson probability for measured counts  $k$  and expected counts  $\lambda$ .

## 6.3 Analysis of the First Tritium Data

During the First Tritium measurement phase the KATRIN experiment was operated at a column density of approximately  $4.45 \cdot 10^{21} \text{ m}^{-2}$  and a DT concentration of 1%. In total we performed 55  $\beta$ -spectrum scanning runs amounting to 109 hours of operation, not including test runs. Of these runs, 28 had a duration of 1 hour and 27 had a duration of 3 hours. In this analysis we will focus on the 3 hour runs due to the higher amount of statistics per run.

We used a MTD designed specifically for the First Tritium phase. While the measurement points start rather deep in the spectrum at 2 keV below the endpoint for the purpose of sterile neutrino search, near the endpoint we measure with smaller step sizes and longer durations to accommodate for the lower decay rate. The MTD is displayed in fig. 6.3. In this analysis, we limit the analysis to an energy window starting from 18100eV, corresponding to energies approximately 400 eV below the endpoint. The larger our selection of data points, the more statistics we have; however the farther away we move from the endpoint, the more systematic uncertainties and corrections we have to consider.

We exclude certain pixels of the FPD from our analysis. These include the outer rings, as they are not fully covered by the magnetic flux tube, as well as some pixels shadowed by the Forward Beam Monitor, a monitoring device that can be inserted after the CPS. While these pixels do contain  $\beta$ -decay information, it is heavily reduced and possibly tainted with systematic uncertainties. Table B.1 shows all settings used in this analysis.

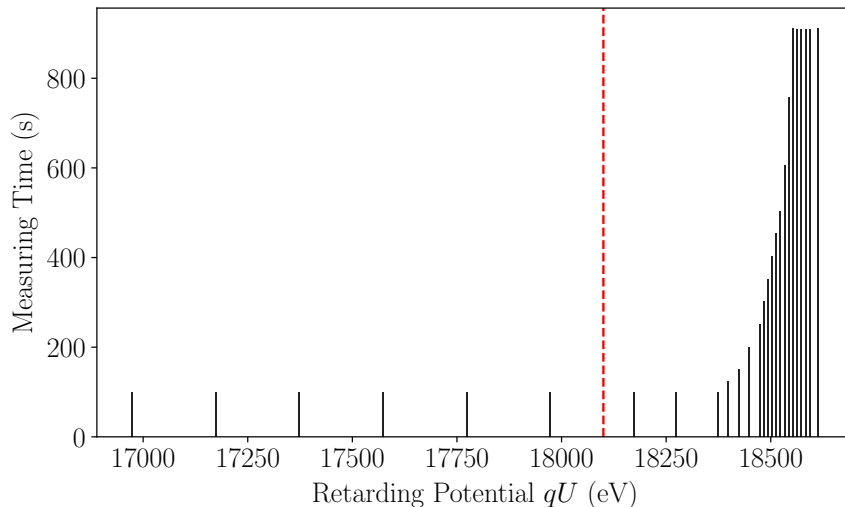


Figure 6.3: Measuring Time Distribution for the 3-hour runs during the First Tritium measurement phase. The red line shows the lower boundary for the energy cut used in this work.

### 6.3.1 Priors

The Bayesian analysis revolves around the selection of priors. In this analysis we want to show the general usability of our models with the First Tritium data, therefore we choose to use mainly non-informative priors. We choose a flat prior for the effective endpoint  $E_0^{\text{eff}}$  and positive definite priors for the normalization  $A$  and the constant background  $C$ . For the neutrino mass, we have multiple options:

The Mainz and Troitsk neutrino mass measurement experiments have set the upper limit of the effective electron neutrino mass to  $2 \text{ eV}/c^2$ . In addition, from neutrino oscillation measurements deliver lower boundaries for neutrino mass eigenstates, from which we can calculate limits for the effective electron neutrino mass. For now we will choose  $0.04 \text{ eV}/c^2$ , which is consistent with the prediction for the lower limit assuming the inverted neutrino mass hierarchy. We will discuss this further in section 6.3.3.

There are two priors that are commonly used in the analysis of the neutrino mass: a flat prior in  $m_\nu$  and a flat prior in  $\log(m_\nu)$ . The former one assigns equal probabilities to all possible values for the neutrino mass. The latter implies not knowing the scale of the neutrino mass and is therefore flat in the logarithm of the neutrino mass, effectively lending a higher probability to smaller neutrino masses.

Another possibility is a flat prior in  $m_\nu^2$ . In the KATRIN experiment, as well as other tritium decay neutrino mass measurements, the neutrino mass squared is the direct observable, not  $m_\nu$ . A prior flat in  $m_\nu^2$  then assigns equal prior probabilities to all observed

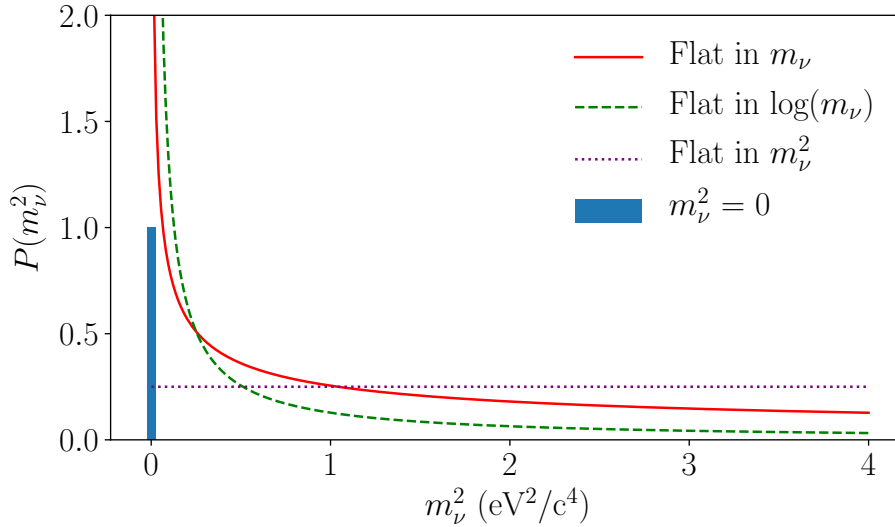


Figure 6.4: Priors on  $m_\nu^2$  used for the analysis. The red curve shows the prior probability distribution function that is flat in the effective electron neutrino mass  $m_\nu$  and the green dashed curve shows the prior probability distribution function that is flat in the logarithm of  $m_\nu$ , implying an agnostic position on the absolute mass scale. The purple dashed curve is the prior probability distribution function that is flat in the observable  $m_\nu^2$ . The blue bar represents the prior probability distribution function that fixes  $m_\nu^2 = 0$ .

values.

The last option is to fix  $m_\nu^2 = 0$ . This implies that we do not account for a neutrino mass in our  $\beta$ -decay measurements. While physically unfeasible, this option is still viable since in our first measurement phase we neither aim for the inference of neutrino mass values, nor is it possible for us to do so due to the limited data available.

Fig. 6.4 plots the priors we used in the subsequent analysis.

### 6.3.2 Uniform Fits

As a first step, we performed a uniform fit as described in 4.2 for run 40667. The main goal of this analysis is to compare the effect of different priors on the neutrino mass, as described in 6.3.1. Fig. 6.5 shows the marginalized posterior distributions for the effective endpoint using different priors and table 6.1 shows the obtained values. Fig. 6.6 shows an example fit. We can see that the shapes of the posteriors do not differ strongly, neither do the inferred values for the effective endpoint.

We can make similar conclusions when comparing the models. Table 6.2 shows the evidence for different priors used. When calculating the Bayes factors, as defined in

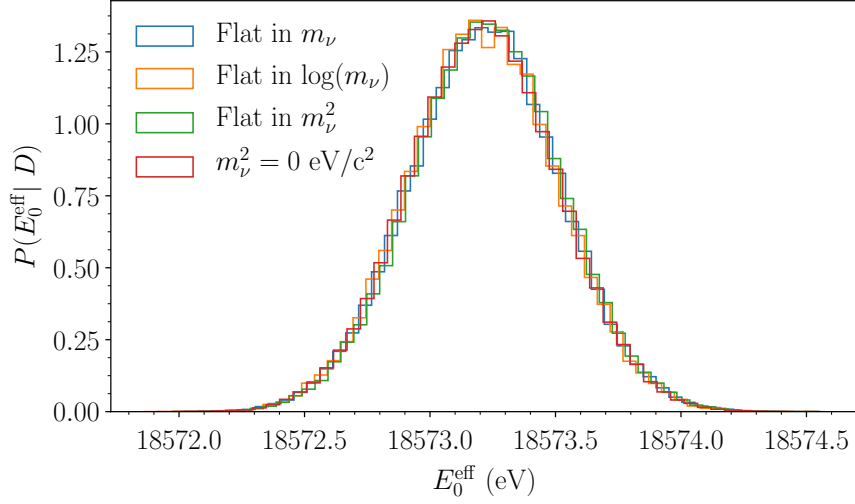


Figure 6.5: Comparison between marginalized posterior probability distributions of the effective endpoint  $E_0^{\text{eff}}$  from a uniform fit using run 40667. The priors used for each posterior are specified.

Table 6.1: 95% credible intervals for the effective endpoint  $E_0^{\text{eff}}$  with different priors from uniform fits using run 40667.

Prior	$E_0^{\text{eff}}$ (eV)
Flat in $m_\nu$	[18572.63, 18573.80]
Flat in $\log(m_\nu)$	[18572.63, 18573.79]
Flat in $m_\nu^2$	[18572.64, 18573.81]
$m_\nu^2 = 0$	[18572.63, 18573.79]

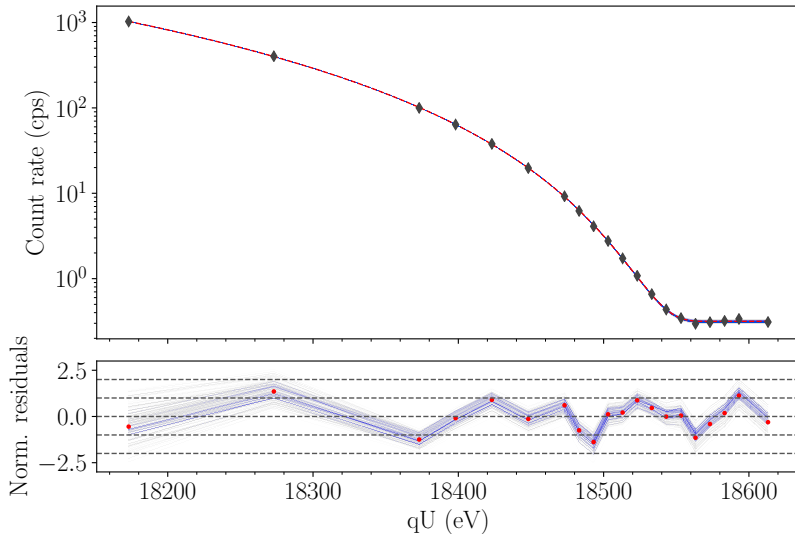


Figure 6.6: Spectrum, model predictions, and residuals from a uniform fit with a flat prior in  $m_\nu$  using run 40667. The blue lines each represent information from a model prediction drawn from the posterior. The red items represent the information from the posterior mean.

section 3.2, we obtain values  $\approx 1$ , pointing to no model being explicitly preferred over the other. This is in accordance to what we expect; due to the scarcity of the data, barely any information about the neutrino mass is available, so it will neither agree nor disagree with the prior.

Table 6.2: Bayesian evidences with different priors from uniform fits using run 40667. The values are all very similar to each other, pointing to no model being favored over another.

Prior	Evidence
Flat in $m_\nu$	0.0033977
Flat in $\log(m_\nu)$	0.0033966
Flat in $m_\nu^2$	0.0033915
$m_\nu^2 = 0$	0.0033970

### 6.3.3 Single-Pixel Fits

We now examine the behavior for the individual pixels to further investigate the effect of different priors and to evaluate whether the effective endpoint  $E_0^{\text{pos}}$  has a positional dependence over the FPD. Fig. 6.7 shows the marginalized posterior distributions for the

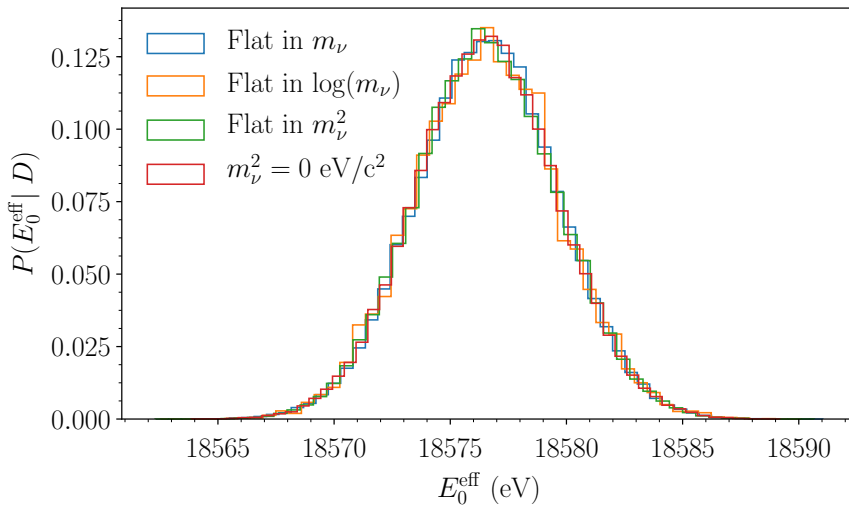


Figure 6.7: Marginalized posterior distribution for the effective endpoint using different priors with a uniform fit for the innermost pixel using run 40667.

effective endpoint using different priors for the innermost pixel as an example. Table 6.3 shows the extracted credible intervals. Again, we can see that there are no big differences when using different priors, as indicated by the posterior shapes and the evidences shown in table 6.4. Fig. 6.8 shows an example fit. Fig. 6.9 shows a heat map of the effective endpoint.

The fits suggest the impact of different priors on  $m_\nu^2$  is minuscule at best. If we choose the lower limit for the effective electron neutrino mass assuming the normal hierarchy, we effectively shift the prior density towards lower values. However we can see, that results using the extreme case of  $m_\nu^2 = 0$  do not differ greatly from results using the other priors. This is why the effect of a change of lower boundaries for the prior in this range is negligible. As the prior flat in  $m_\nu$  makes the least assumptions, we will use it in our subsequent analysis.

Table 6.3: 95% credible intervals for the effective endpoint  $E_0^{\text{eff}}$  with different priors from fits for the innermost pixel using run 40667.

Prior	$E_0^{\text{eff}}$ (eV)
Flat in $m_\nu$	[18570.64, 18582.55]
Flat in $\log(m_\nu)$	[18570.68, 18582.58]
Flat in $m_\nu^2$	[18570.63, 18582.54]
$m_\nu^2 = 0$	[18570.59, 18582.52]

Table 6.4: Bayesian evidences with different priors from fits for the innermost pixel using run 40667. The values are all very similar to each other, pointing to no model being favored over another.

Prior	Evidence
Flat in $m_\nu$	0.010690
Flat in $\log(m_\nu)$	0.010705
Flat in $m_\nu^2$	0.010691
$m_\nu^2 = 0$	0.010653

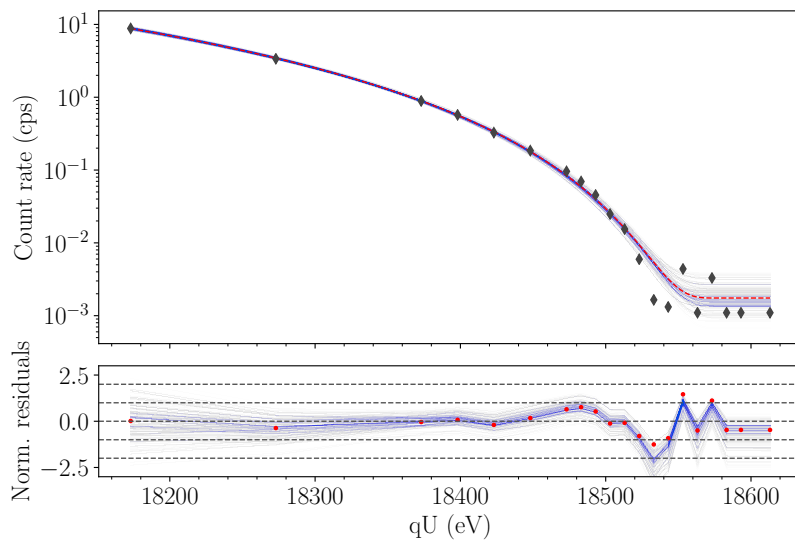


Figure 6.8: Measured spectrum, model predictions, and residuals with a flat prior in  $m_\nu$  for the innermost pixel using run 40667. The blue lines each represent information from a model prediction drawn from the posterior. The red items represent the information from the posterior mean.

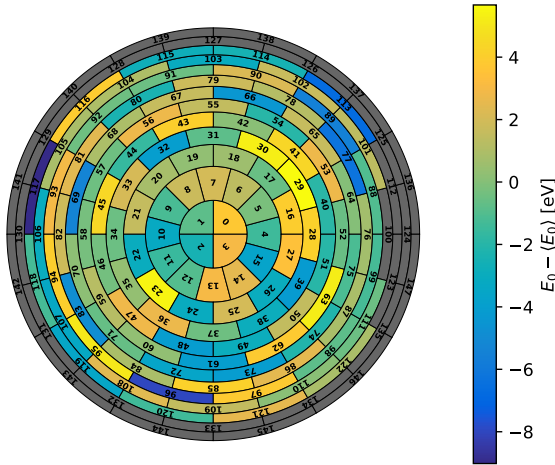


Figure 6.9: Heat map of the effective endpoint with a prior flat in  $m_\nu$  using run 40667. The excluded pixels are greyed out.

### 6.3.4 Multi-Pixel Fits

We will now test the multi-pixel fitting methods. For the chaining method, we start with a flat prior on the effective endpoint and use the marginalized posterior distribution from one analysis and use it as the prior for the subsequent analysis. For the posterior product method, we analyze each pixel separately and combine the marginalized posterior distributions of the endpoint by multiplying them.

We first want to compare the combination techniques to the global fit. Therefore will first limit the number of pixels to 40, which corresponds to the innermost 4 pixels, as well as the first three rings. As mentioned before, the more pixels we analyze in a global fit, the more parameters we have to consider in our model, which slows down our analysis to a great degree. The number we chose allows for a sensible run time ( $\approx 9$  h). Fig. 6.10 shows the marginalized posterior distributions for these methods.

As we can see from the posteriors, the proposed methods are able to replicate the global fit. This is a very satisfying result, as it confirms that our methods can be used for the combination of pixel results. Next we will analyze the full detector. Fig. 6.11 shows the marginalized posterior distributions.

We can see that the posteriors generally agree in their ranges. However, as in the analysis of the krypton measurements, the shape of the posterior product distribution is rather uneven. This is due to the same reason mentioned in section 5.2.4. For the 95% credible interval we obtain  $[18572.26, 18573.52]$  eV using the chaining method and  $[18572.33, 18573.53]$  eV using the posterior product method, showing a good agreement.

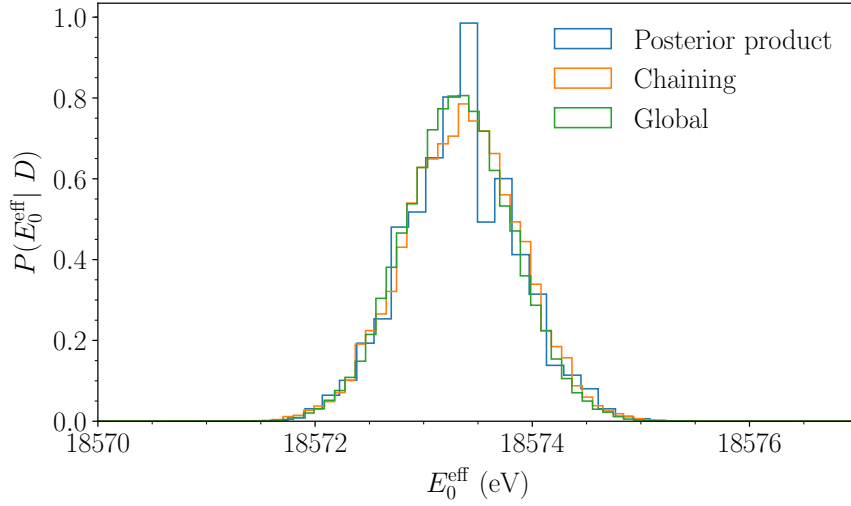


Figure 6.10: Marginalized posterior distributions using a global fit, the chaining method, and the posterior product method for the first 40 pixels using run 40667.

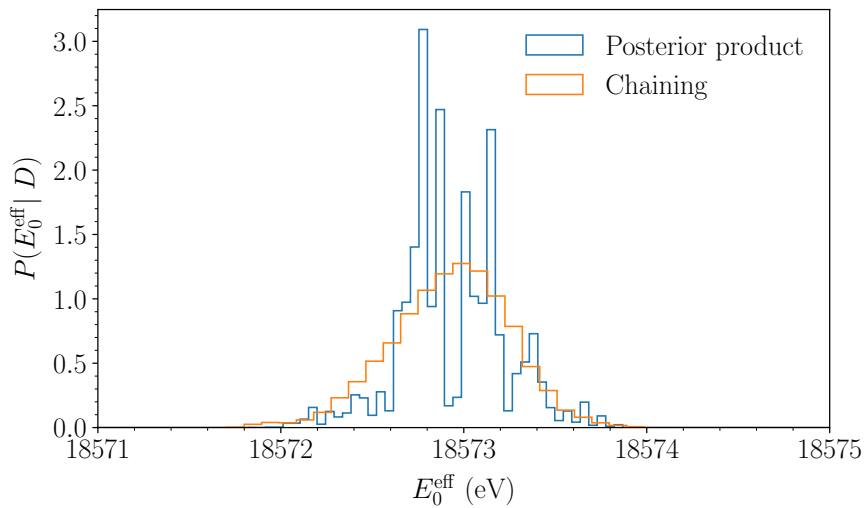


Figure 6.11: Comparison of the marginalized posterior distributions obtained from using the chaining and the posterior product multi-pixel methods using the full detector for run 40667.

## 6.4 Discussion of Systematic Uncertainties

In the wake of the First Tritium measurements, we identified multiple sources of systematic uncertainties. These influence our parameters of interest, namely the effective endpoint  $E_0^{\text{eff}}$  and, due to the high correlation, also the effective electron neutrino mass squared  $m_\nu^2$  in future neutrino mass measurement phases. It is therefore of utmost importance to examine their impact.

### 6.4.1 Column Density and Inelastic Scattering

During the First Tritium measurement phase there was no direct measure of the column density. The column density describes the number of gas molecules per unit area integrated over the entire source length. It correlates highly with the scattering of the electrons and therefore with the response function and thus also with the measurement of the endpoint. As a result, it is important to investigate the impact of its uncertainty on our parameters of interest. Since the column density  $\rho d$  enters our model in a product along with the inelastic scattering cross section  $\sigma$ , we will analyze the product. E.g. for the First Tritium measurements, we estimate a column density  $\rho d = 4.45 \cdot 10^{21} \text{ m}^{-2}$ , and with the inelastic cross section  $\sigma = 3.46 \cdot 10^{-22} \text{ m}^2$  we get  $\rho d \sigma = 1.54$ .

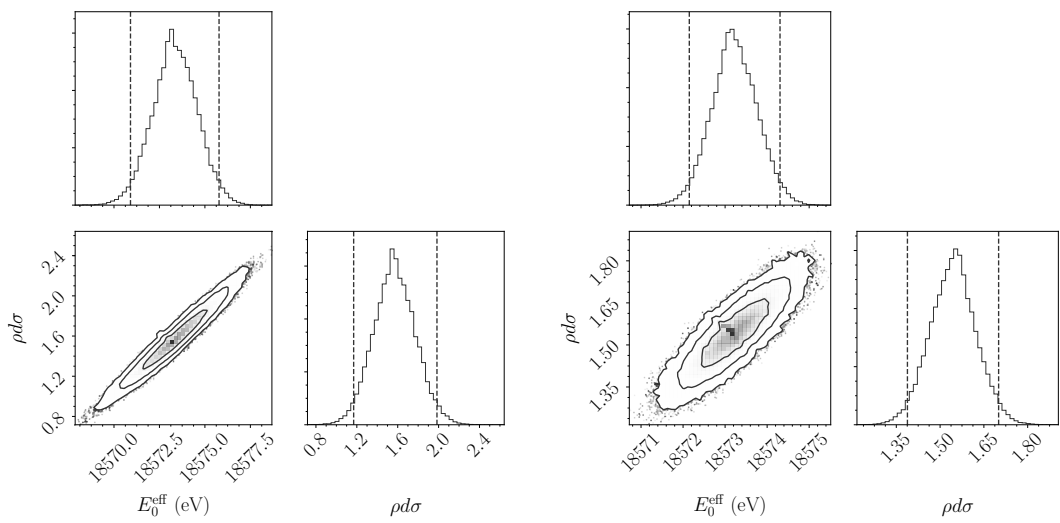
First, we want to see if we can infer a meaningful value by fitting the column density. We therefore set a positive definite prior on  $\rho d \sigma$ . Fig. 6.12a shows the marginalized posterior distributions. The distribution for  $\rho d \sigma$  seems well-behaved and we can infer a 95% credible interval of [1.23, 1.91], corresponding with  $[3.57, 5.53] \cdot 10^{22} \text{ m}^2$  on  $\rho d$ . This is consistent with our estimation of  $\rho d \sigma$ .

We could however obtain estimates from simulations using indirect measurements. These assume  $\rho d$  to be at  $4.45 \cdot 10^{21} \text{ m}^{-2}$  with relative uncertainties of  $[-5.31\%, +4.69\%]$  [Hei18]. We will use a conservative symmetric error with the larger value 5.31%. As there is also an error of 2% on the inelastic cross section, we add those uncertainties in quadrature and obtain a combined error of 5.67%. Using this information, we apply a Gaussian prior on  $\rho d \sigma$ . Fig. 6.12b shows the posterior distributions.

From this fit we also obtain a 95% credible interval on  $\rho d \sigma$  of [1.41, 1.68]. Fig. 6.13 shows a knowledge update as well as a comparison with a flat prior on  $\rho d \sigma$ . Fig. 6.14 shows a comparison of marginalized posterior distributions using different priors for  $\rho d \sigma$ .

### 6.4.2 FSD Onset

The daughter molecule can assume an electronic ground or excited state. The ratio of probabilities between the electronic ground and excited states is called the FSD onset. We normalize it to the range  $[-1, 1]$ , where 1 corresponds to having only electronic ground states,  $-1$  corresponds to only electronic excited states, and 0 corresponds to the theoretical prediction. In this part, we first want to show that in our short measurement



(a) Flat prior

(b) Informative Gaussian prior with a 5.31% relative width centered around the run summary value.

Figure 6.12: Marginalized posterior distributions of the effective endpoint and  $\rho d\sigma$  for different priors on  $\rho d\sigma$  from a uniform fit with run 40667. The dashed lines show the 95% credible intervals. Using a prior constrains the width of  $\rho d\sigma$  and also the contributed width of the effective endpoint  $E_0^{\text{eff}}$  due to their correlation.

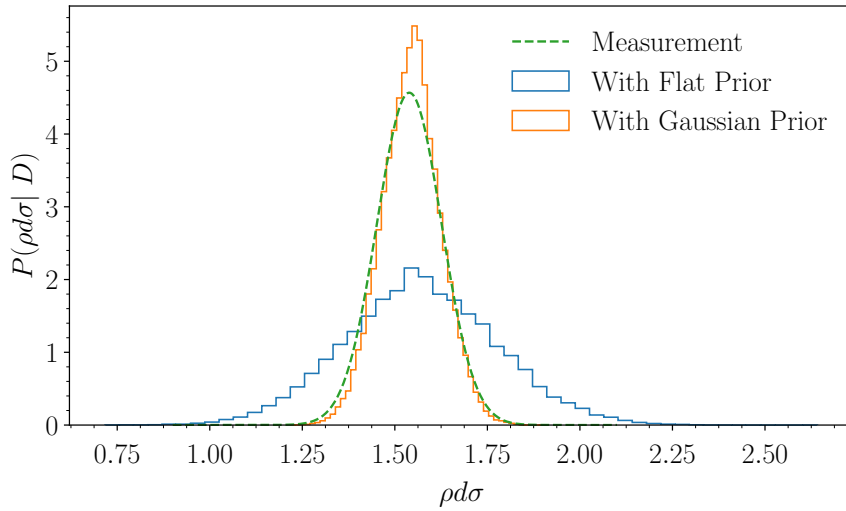


Figure 6.13: Comparison and knowledge update plot of  $\rho d\sigma$  for uniform fits using run 40667. The 'Measurement' curve shows a Gaussian distribution centered around our estimate for  $\rho d\sigma$  with a 5.67% combined uncertainty, representing our prior information. Using it as a prior probability distribution function constrains the uncertainty of  $\rho d\sigma$ .

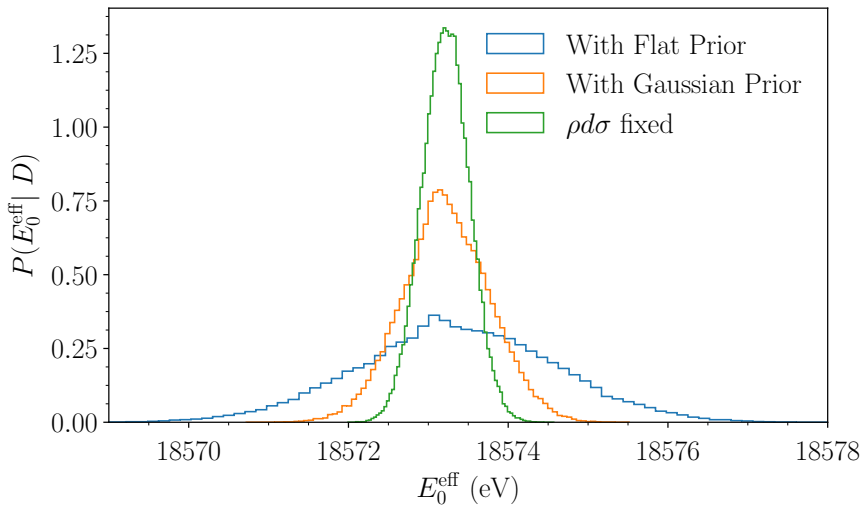


Figure 6.14: Comparison of the effective endpoint  $E_0^{\text{eff}}$  for different priors on  $\rho d\sigma$  for uniform fits using run 40667. A higher uncertainty in  $\rho d\sigma$  contributes to a higher uncertainty in  $E_0^{\text{eff}}$ . The Gaussian prior has a relative width of 5.67%, centered around our estimate for  $\rho d\sigma$ .

phase we already have indications for detecting the excited final states. We perform fits both including and excluding the electronic excited states. We then compute the Bayes evidence. Table 6.5 shows the results.

Table 6.5: Bayesian evidence for different final state distributions for a uniform fit using run 40667. The first case describes a fit with the weighting predicted by theory of the electronic final states, the second one describes a fit excluding the electronic excited final states, and the last one describes a fit excluding the electronic excited final states and considers a relative uncertainty of 5.67% on  $\rho d\sigma$  as described in section 6.4.1. Both including and excluding our main systematic uncertainty we obtain a Bayes factor that implies "extreme evidence" for seeing the excited states.

FSD used	Evidence
Theoretical prediction	0.0033978
Ground states only	0.0000132
Ground states only & uncertainty on $\rho d\sigma$	0.0000067

We obtain a Bayes factor of  $K = 261$ , which implies "extreme evidence" for seeing the excited states. This even holds true when we include the relative Gaussian uncertainty of 5.67% on  $\rho d\sigma$  (see 6.4.1): Performing the fit and comparing it to the theoretical prediction gives us a Bayes factor of  $K = 509$ . We can therefore conclude that in this phase we are already able to detect the electronic excited states.

Next, we want to test whether we can infer a new value on the FSD onset from our data alone. For that, we set a flat prior on the FSD onset. Fig. 6.15 shows the marginalized posterior distribution.

We obtain a mean for the FSD onset of  $-0.075$  with the 95% credible interval of  $[-0.521, 0.334]$  from the marginalized posterior distribution. The mean is very close to the weighting predicted by theoretical calculations and assigns a slightly higher probability to the electronic excited states. If we compute another Bayes factor comparing the fit using a flat prior for the FSD onset to the fit with the theoretical prediction, we obtain  $K = 1.02$ . The value implies that there is no preference for either models in particular. This means, based on this data, we do not obtain a better value for the FSD onset.

### 6.4.3 Full Systematics Treatment

We now apply all major systematic uncertainties. Table 6.6 shows the sources of systematic uncertainties and their associated relative errors. For each we apply a Gaussian prior centered around the run summary value with the width specified in table 6.6. Fig. 6.16 shows the marginalized posterior distributions, and for  $E_0^{\text{eff}}$  we obtain a 95% credible interval of  $[18572.09, 18574.37]$  eV. Fig. 6.17 shows a comparison of model predictions including and

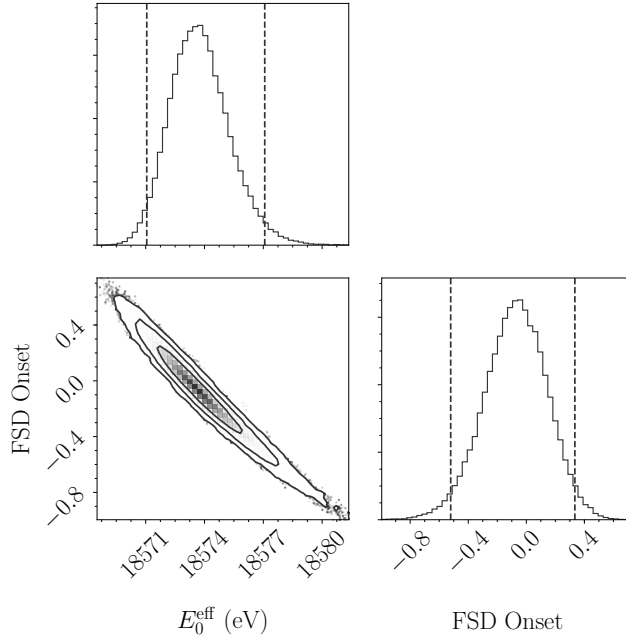


Figure 6.15: Marginalized posterior distributions using a flat prior on the FSD onset for a uniform fit using run 40667.

excluding systematic uncertainties. We can see that the systematic uncertainties mainly affect the model prediction for measurement points deeper in the spectrum: The farther away from the endpoint, the higher the model uncertainty becomes. Close to the endpoint however the spectrum is dominated by statistical errors. Fig. 6.18 shows a comparison of credible intervals considering different systematical uncertainties and their treatment.

Table 6.6: Table of systematic uncertainties used for the full treatment analysis. The absolute values are provided by the run summary or, in the case of  $\rho d$ , external estimates.

Setting	Relative systematic uncertainty
Column density $\rho d$	5.31%
Inelastic scattering cross section $\sigma$	2%
FSD onset	3%
Magnetic fields $B_S, B_{\max}, B_{\text{ana}}$	2% (each)

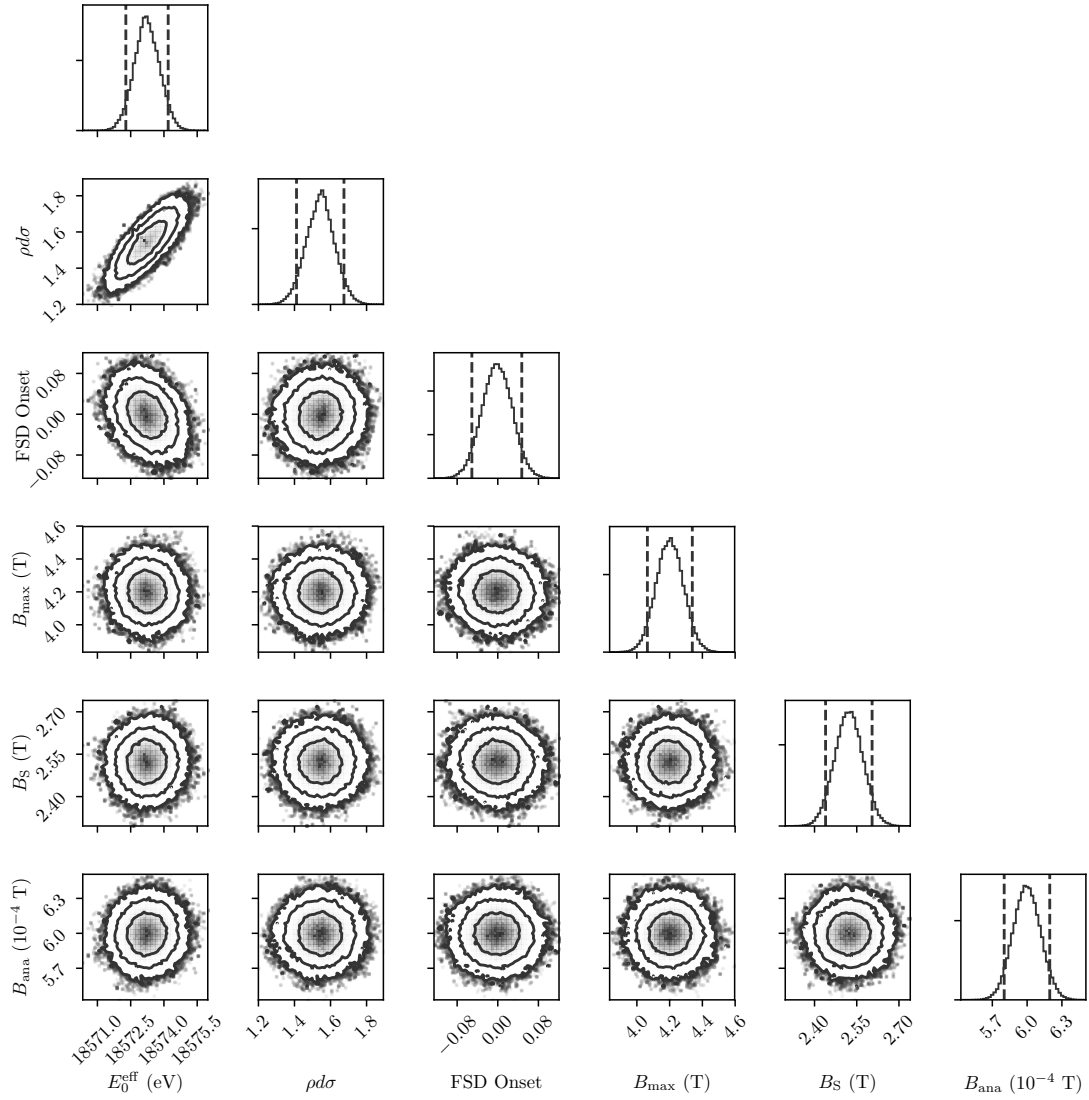


Figure 6.16: Marginalized posterior distributions for a uniform fit including all systematic uncertainties using a flat prior in  $m_\nu$  for run 40667. The main contribution to the systematic uncertainty comes from  $\rho d\sigma$ , the other effects have a low correlation or are constrained by their respective prior. We obtain a 95% CI on  $E_0^{\text{eff}} = [18572.09, 18574.37]$  eV.

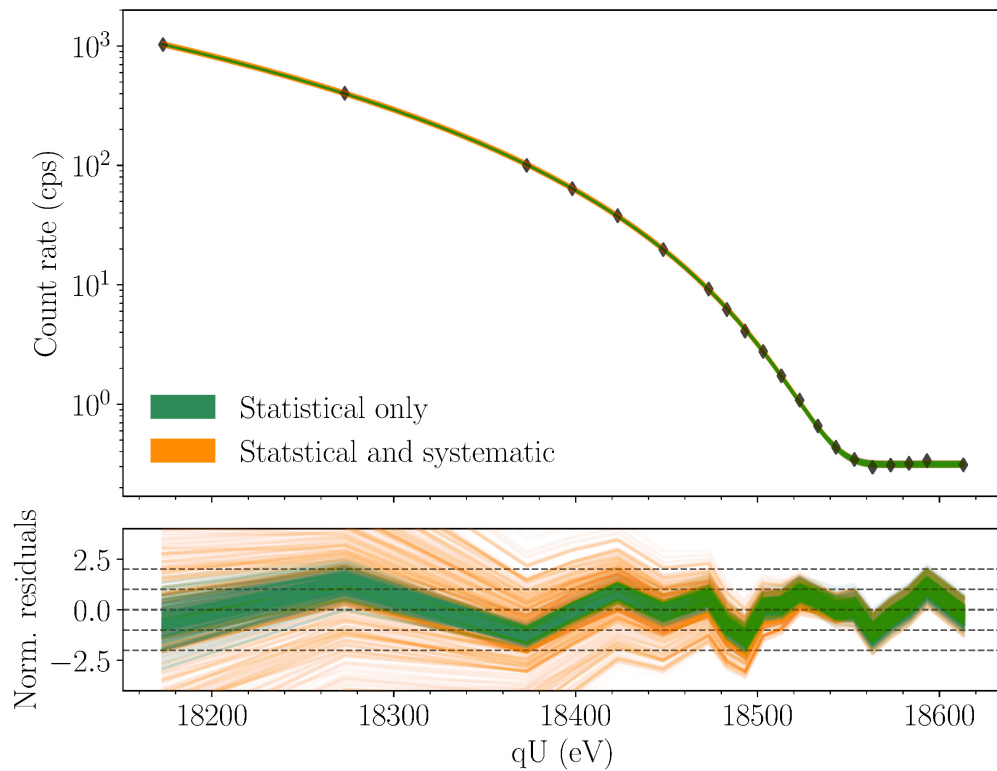


Figure 6.17: Comparison of model predictions for uniform fits with and without systematic uncertainties using run 40667. The green and orange lines represent model predictions drawn from posterior distributions obtained from fits excluding and including systematic errors respectively. The model prediction from the posterior using a fit including systematic uncertainties indicate that the uncertainty mostly affects our model calculation farther away from the endpoint.

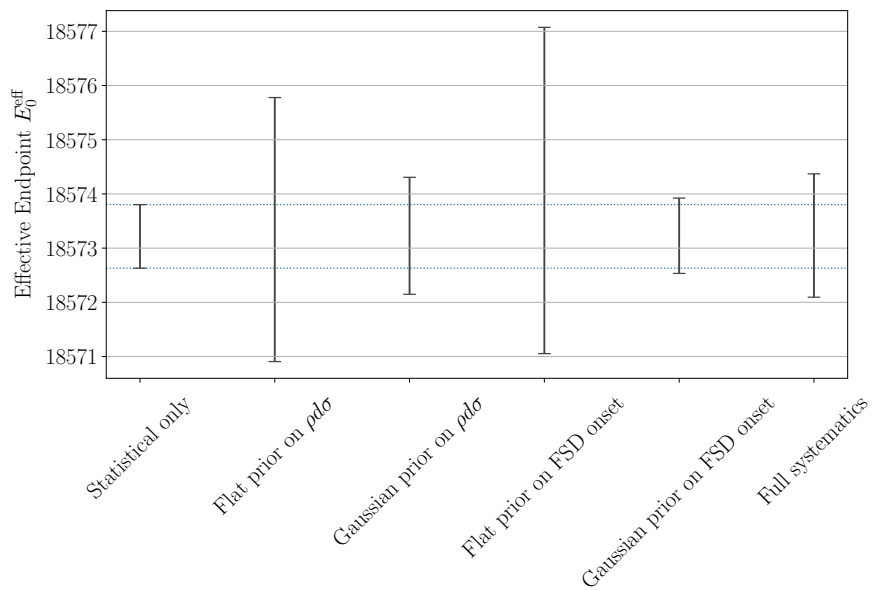


Figure 6.18: Comparison of 95% credible intervals for different systematical uncertainties under different priors for a uniform fit using run 40667. When an informative prior was used, they follow table 6.6. The dotted lines indicate the extent of the statistical uncertainty.

## Chapter 7

# Conclusion

In this work we investigated the possibilities of using the Bayesian school of analysis to examine the first KATRIN data. To this end, the publicly available Bayesian Analysis tool kit (BAT) was used. The focus of this work was to 1) test different methods to combine the data of all 148 pixels of the focal plane detector and 2) to investigate the impact of systematic uncertainties.

A simultaneous fit of all pixels, the so-called global multi-pixel fit, involves the sampling of a high-dimensional ( $> 300$ ) posterior distribution, which depicts a problem for the Metropolis-Hastings algorithm, which we used in this work. For this reason two alternative approaches were developed in the framework of this thesis: the chaining method and the posterior product. Based on both krypton and tritium data we could show that both methods lead to comparable results and agree with the global multi-pixel technique.

The Bayesian approach is highly suited for the treatment of systematic uncertainties. In this thesis systematic uncertainties were included as additional nuisance parameters in the likelihood function and different prior knowledge on their value was exploited. In particular, the effect of the high voltage ripple on the line width was investigated. Moreover, using prior knowledge on the high voltage ripple and line width, we extracted the credible interval of the energy resolution of the KATRIN main spectrometer from the krypton data. In the case of the First Tritium data set we investigated two main systematics, the column density and the FSD onset. We discussed the effect of the uncertainty of these parameter on the effective endpoint as well as and the possibility to learn about these parameters from the spectral data. Most notably, we could show that the FSD onset is clearly detectable with the First Tritium data, with a Bayes factor of  $K = 509$ , implying "extreme evidence".

The analysis performed in this work serves as an important basis for the neutrino mass measurement, which is scheduled to start in March 2019.

## 7.1 Outlook

The main objective of this work is to show the general usability of the BAT and the Bayesian school in general in the KATRIN experiment. Following further steps are foreseen for upcoming neutrino mass measurements.

### 7.1.1 Other systematics

We identified other systematic uncertainties during the First Tritium measurements that were not included in the analysis in this work. However we do plan to incorporate these, as they will be of importance during the neutrino mass measurements. The systematic uncertainties include a fluctuation of the DT concentration between measurement points in the spectrum and a uncertainty in the shape of the FSD. These uncertainties are difficult to parametrize. However we do have a method of handling them, the so-called Monte Carlo propagation:

We perform many analyses where for each run we alter the model according to our systematic uncertainties. E.g. we randomize the setting for the DT concentration for each measurement point, or we randomize the spectrum of the FSD. We then obtain a set of MCMC samples for each iteration which we then can just bin in a histogram similar to our regular analysis.

### 7.1.2 BAT-2 & Hamiltonian Monte Carlo

A large caveat of the Metropolis-Hastings algorithm is that it fails at a large number of parameters ( $\gg 10$ ) since the proposal of new points depends mostly on random number generation. The Markov chain can therefore 'get lost' in low probability spaces, especially in higher dimensions. An alternative is Hamiltonian Monte Carlo. This method additionally uses gradient information to optimize the chain proposal.

BAT-2 is the successor of BAT in development, based on the *Julia* language [Bez+17]. Hamiltonian Monte Carlo is a highly demanded feature and will be implemented soon. With it we will prospectively be able to do a global multi-pixel fit for the full detector.

### 7.1.3 Bayesian Run Combining

For now, we have only focused on one run, or spectral scan, at a time. Obviously, in the future, we will have a plethora, which we will have to combine to extract physical information. While we have trust in our model, we cannot exclude the existence of systematic uncertainties between runs, which we then have to take into account. It will be a task to contemplate methods how to combine them, possibly under a Bayesian framework, similarly to the pixel combining.

#### 7.1.4 Neural Network

The calculation of the KATRIN response function is very expensive. Especially nested integrals require heavy computation. For regular analysis we handle this by pre-calculating and caching the model. This is however not possible if we have to analyze systematics where the response function has to be recalculated. One way we can deal with this is by using neural networks for approximation.

Neural networks, especially in conjunction with modern processing technology, are a very fast method for regression. We compute samples of the function we want to replicate, e.g. the integrated spectrum or the response function, with which we can train the neural network.

# Appendices

## Appendix A

# Additional Content Concerning the Krypton Analysis

### A.1 Settings

Table A.1: Settings used for the gaseous krypton analysis.

Setting	(Provided) Value
Runs	33196 – 33200
Excluded pixels	124 – 126, 129, 136 – 141, 147
Retarding potential window	[30465, 30500] eV
Source temperature	100 K
$B_{\max}$	4.2 T
$B_{\text{S}}$	2.52 T
$B_{\text{ana}}$	$\sim 2.7 \cdot 10^{-4}$ T
High voltage ripple amplitude $A_{\text{HV}}$	208 mV
Number of Markov chains	8
Number of iterations per chain	100000

## A.2 Discussion of Systematic Uncertainties

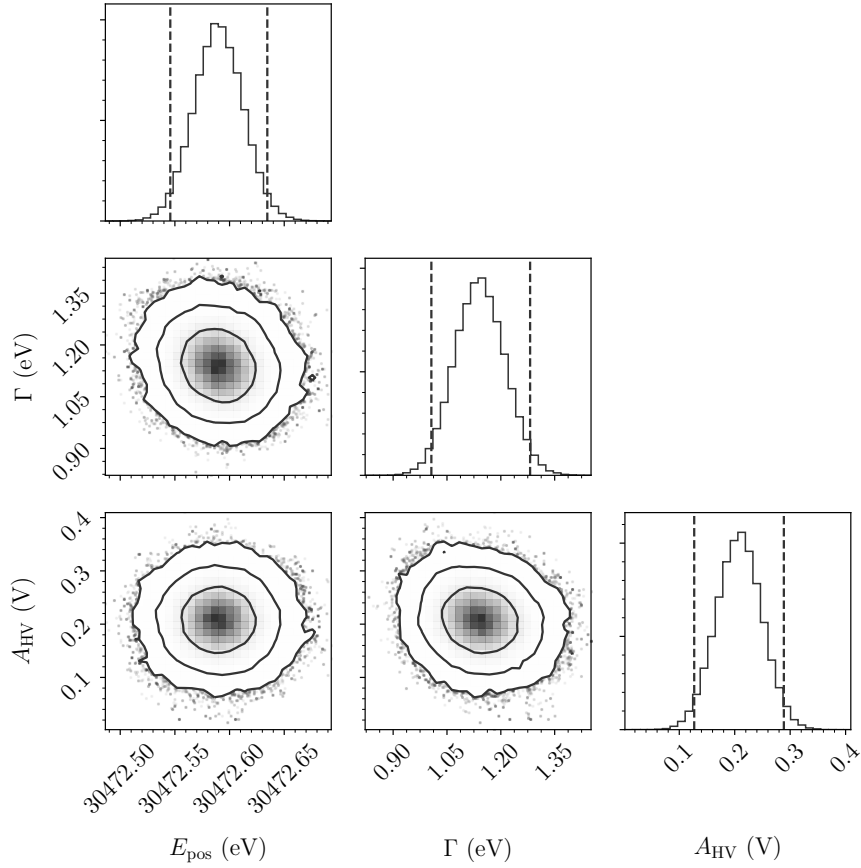
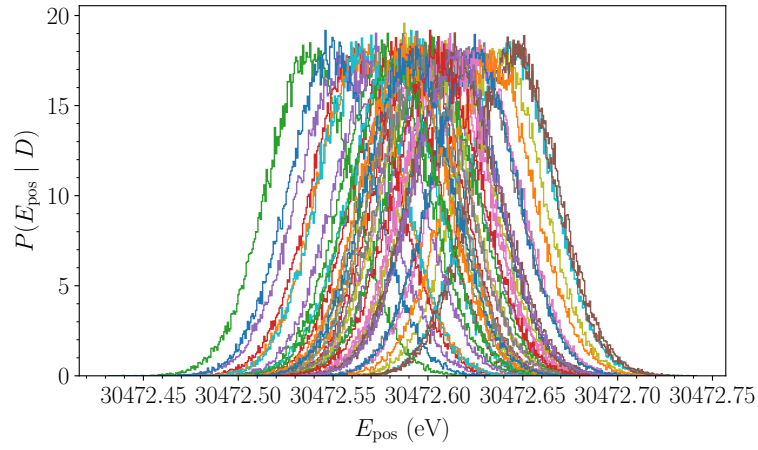
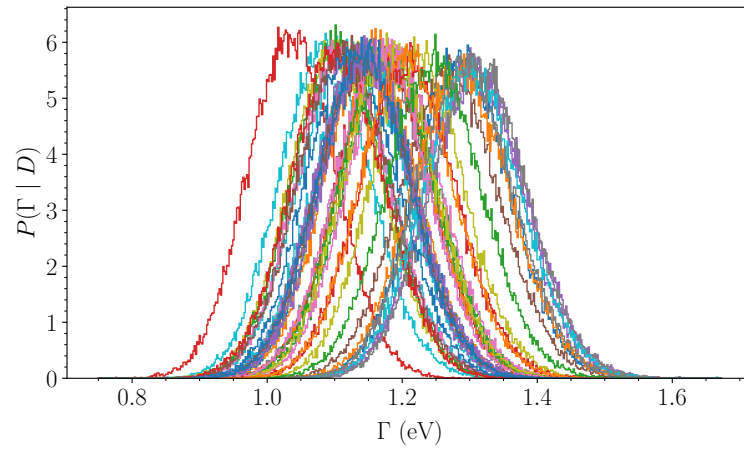


Figure A.1: Marginalized posterior distributions for a fit of the innermost pixel using a Gaussian prior with a 20% relative width around the experimental measurement of 208 mV on the high voltage ripple amplitude  $A_{\text{HV}}$ . The correlation between the line width  $\Gamma$  and  $A_{\text{HV}}$  is suppressed due to the constraint of the prior on  $A_{\text{HV}}$ .

### A.3 Multi-Pixel Fits



(a) Line position  $E_{\text{pos}}$ .



(b) Line width  $\Gamma$ .

Figure A.2: Marginalized posterior distributions for the first 40 pixels with statistical errors only.

## Appendix B

# Additional Content Concerning the Tritium Analysis

### B.1 Prior Probability Distribution Functions for $m_\nu^2$

For the difference of the effective electron neutrino mass squared boundaries  $\Delta m_\nu^2 = m_{\nu, \text{ upper}}^2 - m_{\nu, \text{ lower}}^2$  and  $m_\nu^2 > 0$  (excluding the last case).

Flat in  $m_\nu$ :

$$P(m_\nu^2) = \frac{1}{2\Delta m_\nu^2} \cdot \frac{1}{\sqrt{m_\nu^2}}. \quad (\text{B.1})$$

Flat in  $\log(m_n u)$ :

$$P(m_\nu^2) = \frac{1}{\Delta m_\nu^2} \cdot \frac{1}{m_\nu^2}. \quad (\text{B.2})$$

Flat in  $m_\nu^2$ :

$$P(m_\nu^2) = \frac{1}{\Delta m_\nu^2}. \quad (\text{B.3})$$

$m_\nu^2 = 0$ :

$$P(m_\nu^2) = \delta(m_\nu^2). \quad (\text{B.4})$$

## B.2 Settings

Table B.1: Settings used for the First Tritium analysis.

Setting	(Provided) Value
Run summary version	2f
Excluded pixels	100, 112, 123 – 147
Retarding potential window	$qU > 18100$ eV
DT concentration	1%
Column density $\rho d$	$4.45 \cdot 10^{21}$ m <sup>-2</sup>
Inelastic scattering cross section $\sigma$	$3.46 \cdot 10^{-22}$ m <sup>2</sup>
Number of electron scatterings	7
$B_{\max}$	4.2 T
$B_S$	2.52 T
$B_{\text{ana}}$	$\sim 6 \cdot 10^{-4}$ T
Detector efficiency	95%
Number of Markov chains	8
Number of iterations per chain	125000

### B.3 Multi-Pixel Fits

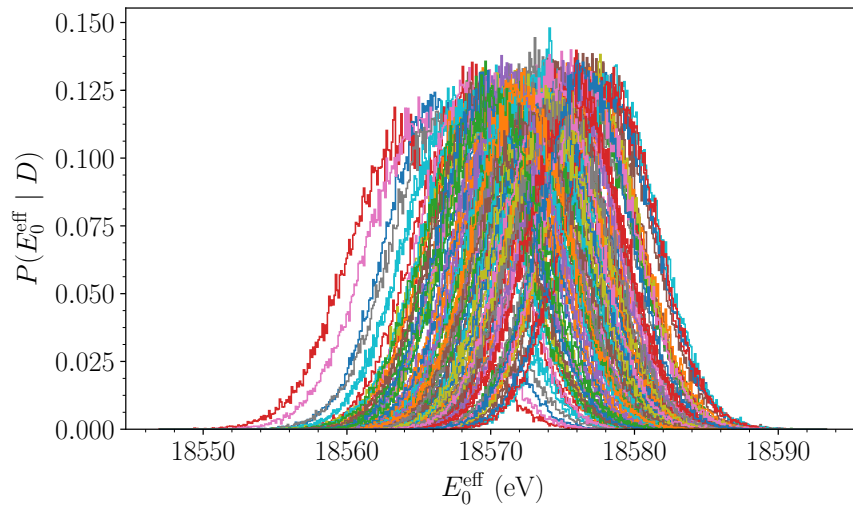


Figure B.1: Marginalized posterior distributions for all analyzed pixels with statistical errors only for run 40667.

## B.4 Treatment of Systematic Uncertainties

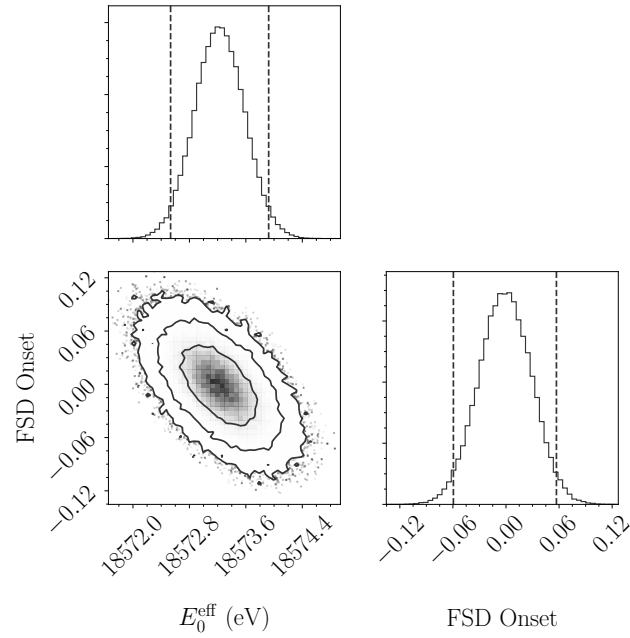


Figure B.2: Marginalized posterior distributions for a uniform fit with a Gaussian prior with a relative width of 3% centered around the theoretical prediction. The 95% credible intervals are  $E_0^{\text{eff}} = [18572.53, 18573.92]$  and FSD onset =  $[-0.0593, 0.057]$ .

# Bibliography

- [Ahm+01] Q. R. Ahmad et al. “Measurement of the Rate of  $\nu_e + d \rightarrow p + p + e^-$  Interactions Produced by  $^8B$  Solar Neutrinos at the Sudbury Neutrino Observatory”. In: *Phys. Rev. Lett.* 87 (7 July 2001), p. 071301. DOI: 10.1103/PhysRevLett.87.071301 (p. 4).
- [Ams+15] J.F. Amsbaugh et al. “Focal-plane detector system for the KATRIN experiment”. In: *Nuclear Instruments and Methods in Physics Research Section A: Accelerators, Spectrometers, Detectors and Associated Equipment* 778 (Apr. 2015), pp. 40–60. DOI: 10.1016/j.nima.2014.12.116 (p. 9).
- [Are+18] M. Arenz et al. “Calibration of high voltages at the ppm level by the difference of  $^{83m}Kr$  conversion electron lines at the KATRIN experiment”. In: *The European Physical Journal C* 78.5 (May 2018). DOI: 10.1140/epjc/s10052-018-5832-y (p. 30).
- [Ase+11] V. N. Aseev et al. “Upper limit on the electron antineutrino mass from the Troitsk experiment”. In: *Physical Review D* 84.11 (Dec. 2011). DOI: 10.1103/physrevd.84.112003 (p. 5).
- [Ase+00] V.N. Aseev et al. “Energy loss of 18 keV electrons in gaseous T and quench condensed D films”. In: *The European Physical Journal D - Atomic, Molecular, Optical and Plasma Physics* 10.1 (Mar. 2000), pp. 39–52. ISSN: 1434-6079. DOI: 10.1007/s100530050525 (p. 11).
- [Bab14] Martin Babutzka. “Design and development for the Rearsection of the KATRIN experiment”. PhD thesis. 2014 (p. 7).
- [Beh+17] J. Behrens et al. “A pulsed, mono-energetic and angular-selective UV photoelectron source for the commissioning of the KATRIN experiment”. In: *The European Physical Journal C* 77.6 (June 2017), p. 410. ISSN: 1434-6052. DOI: 10.1140/epjc/s10052-017-4972-9 (p. 8).
- [Bez+17] Jeff Bezanson et al. “Julia: A Fresh Approach to Numerical Computing”. In: *SIAM Review* 59.1 (Jan. 2017), pp. 65–98. DOI: 10.1137/141000671 (p. 56).

- [Bor06] L. Bornschein. “Measurements with the KATRIN pre-spectrometer”. In: *Progress in Particle and Nuclear Physics* 57.1 (July 2006), pp. 49–57. DOI: 10.1016/j.ppnp.2005.12.011 (p. 8).
- [CKK09] Allen Caldwell, Daniel Kollár, and Kevin Kröninger. “BAT – The Bayesian analysis toolkit”. In: *Computer Physics Communications* 180.11 (2009), pp. 2197–2209. ISSN: 0010-4655. DOI: <https://doi.org/10.1016/j.cpc.2009.06.026> (p. 16).
- [Cho18] Woonqook Choi. *Alignment Estimation via Krypton Line Position Deviation*. URL: <https://fuzzy.fzk.de/bscw/bscw.cgi/1196645>. KATRIN Collaboration Meeting #34 Talk. Feb. 2018 (p. 25).
- [Cle+98] Bruce T. Cleveland et al. “Measurement of the Solar Electron Neutrino Flux with the Homestake Chlorine Detector”. In: *The Astrophysical Journal* 496.1 (Mar. 1998), pp. 505–526. DOI: 10.1086/305343 (p. 3).
- [Cow+56] C. L. Cowan et al. “Detection of the Free Neutrino: a Confirmation”. In: *Science* 124.3212 (July 1956), pp. 103–104. DOI: 10.1126/science.124.3212.103 (p. 3).
- [Dan+62] G. Danby et al. “Observation of High-Energy Neutrino Reactions and the Existence of Two Kinds of Neutrinos”. In: *Physical Review Letters* 9.1 (July 1962), pp. 36–44. DOI: 10.1103/physrevlett.9.36 (p. 3).
- [DHH68] Raymond Davis, Don S. Harmer, and Kenneth C. Hoffman. “Search for Neutrinos from the Sun”. In: *Physical Review Letters* 20.21 (May 1968), pp. 1205–1209. DOI: 10.1103/physrevlett.20.1205 (p. 3).
- [DT08] Natasha Doss and Jonathan Tennyson. “Excitations to the electronic continuum of  $^3\text{HeT}$  in investigations of T2  $\beta$ -decay experiments”. In: *Journal of Physics B: Atomic, Molecular and Optical Physics* 41.12 (June 2008), p. 125701. DOI: 10.1088/0953-4075/41/12/125701 (p. 36).
- [Dos+06] Natasha Doss et al. “Molecular effects in investigations of tritium molecule  $\beta$ decay endpoint experiments”. In: *Physical Review C* 73.2 (Feb. 2006). DOI: 10.1103/physrevc.73.025502 (p. 36).
- [Ell+17] E. Ellinger et al. “Monitoring the KATRIN source properties within the beamline”. In: *Journal of Physics: Conference Series* 888 (Sept. 2017), p. 012229. DOI: 10.1088/1742-6596/888/1/012229 (p. 13).
- [FS03] Y. Farzan and A.Yu. Smirnov. “On the effective mass of the electron neutrino in beta decay”. In: *Physics Letters B* 557.3-4 (Apr. 2003), pp. 224–232. DOI: 10.1016/s0370-2693(03)00207-7 (p. 35).
- [Fer34] E. Fermi. “Versuch einer Theorie der  $\beta$ -Strahlen. I”. In: *Zeitschrift für Physik* 88.3-4 (Mar. 1934), pp. 161–177. DOI: 10.1007/bf01351864 (p. 3).

- [FW03] B. Flatt and J. Wolf. “Design of the KATRIN pre-spectrometer”. In: *Nuclear Physics B - Proceedings Supplements* 118 (Apr. 2003), p. 483. DOI: 10.1016/S0920-5632(03)01373-2 (p. 8).
- [For16] Daniel Foreman-Mackey. “corner.py: Scatterplot matrices in Python”. In: *The Journal of Open Source Software* 24 (2016). DOI: 10.21105/joss.00024 (p. 15).
- [Fur+17] Daniel Furse et al. “Kassiopeia: a modern, extensible C++ particle tracking package”. In: *New Journal of Physics* 19.5 (May 2017), p. 053012. DOI: 10.1088/1367-2630/aa6950 (p. 9).
- [Gan+16] A. Gando et al. “Search for Majorana Neutrinos Near the Inverted Mass Hierarchy Region with KamLAND-Zen”. In: *Physical Review Letters* 117.8 (Aug. 2016). DOI: 10.1103/physrevlett.117.082503 (p. 5).
- [Gil+10] Woosik Gil et al. “The Cryogenic Pumping Section of the KATRIN Experiment”. In: *IEEE Transactions on Applied Superconductivity* 20.3 (June 2010), pp. 316–319. DOI: 10.1109/tasc.2009.2038581 (p. 8).
- [Hei18] Florian Heizmann. *Calculations of Column Densities from Throughput, Run-Summary etc.* URL: <https://neutrino.ikp.kit.edu/katrin/images/8/89/2018-07-19-ThroughputColdensETC.pdf>. KATRIN Analysis Week Munich 2018 Talk. July 2018 (p. 47).
- [Ha17] Florian Heizmann and Hendrik Seitz-Moskaliuk and. “The Windowless Gaseous Tritium Source (WGTS) of the KATRIN experiment”. In: *Journal of Physics: Conference Series* 888 (Sept. 2017), p. 012071. DOI: 10.1088/1742-6596/888/1/012071 (p. 8).
- [Hos+06] J. Hosaka et al. “Solar neutrino measurements in Super-Kamiokande-I”. In: *Physical Review D* 73.11 (June 2006). DOI: 10.1103/physrevd.73.112001 (p. 4).
- [Jef61] H. Jeffreys. *Theory of Probability*. Third. Oxford, England: Oxford, 1961 (p. 16).
- [Kar18] Christian Karl. “Analysis of the First Tritium Data of the KATRIN Experiment”. MA thesis. Max Planck Institute for Physics, Technical University Munich, Oct. 2018 (p. 38).
- [KK05] KATRIN Collaboration and KATRIN Collaboration. *KATRIN design report 2004*. Tech. rep. 51.54.01; LK 01. Forschungszentrum, Karlsruhe, 2005. 245 pp. (p. 7).
- [Kod+01] K. Kodama et al. “Observation of tau neutrino interactions”. In: *Physics Letters B* 504.3 (Apr. 2001), pp. 218–224. DOI: 10.1016/S0370-2693(01)00307-0 (p. 3).

- [Kra+05] Ch Kraus et al. “Final results from phase II of the Mainz neutrino mass search in tritium  $\{\beta\}$ decay”. In: *The European Physical Journal C* 40.4 (Apr. 2005), pp. 447–468. DOI: 10.1140/epjc/s2005-02139-7 (p. 5).
- [LW14] M.D. Lee and E.J. Wagenmakers. *Bayesian Cognitive Modeling: A Practical Course*. Cambridge University Press, 2014. ISBN: 9781107653917 (p. 16).
- [LS85] V.M. Lobashev and P.E. Spivak. “A method for measuring the electron antineutrino rest mass”. In: *Nuclear Instruments and Methods in Physics Research Section A: Accelerators, Spectrometers, Detectors and Associated Equipment* 240.2 (Oct. 1985), pp. 305–310. DOI: 10.1016/0168-9002(85)90640-0 (p. 8).
- [Luk+12] S. Lukić et al. “Measurement of the gas-flow reduction factor of the KATRIN DPS2-F differential pumping section”. In: *Vacuum* 86.8 (Feb. 2012), pp. 1126–1133. DOI: 10.1016/j.vacuum.2011.10.017 (p. 8).
- [Luo+06] X. Luo et al. “Monte Carlo simulation of gas flow through the KATRIN DPS2-F differential pumping system”. In: *Vacuum* 80.8 (June 2006), pp. 864–869. DOI: 10.1016/j.vacuum.2005.11.044 (p. 8).
- [MNS62] Ziro Maki, Masami Nakagawa, and Shoichi Sakata. “Remarks on the Unified Model of Elementary Particles”. In: *Progress of Theoretical Physics* 28.5 (Nov. 1962), pp. 870–880. DOI: 10.1143/ptp.28.870 (p. 4).
- [McC15] E.A. McCutchan. “Nuclear Data Sheets for A = 83”. In: *Nuclear Data Sheets* 125 (Mar. 2015), pp. 201–394. DOI: 10.1016/j.nds.2015.02.002 (pp. 21, 22).
- [OW08] E W Otten and C Weinheimer. “Neutrino mass limit from tritium  $\beta$ decay”. In: *Reports on Progress in Physics* 71.8 (July 2008), p. 086201. DOI: 10.1088/0034-4885/71/8/086201 (p. 35).
- [P A+16] and P. A. R. Ade et al. “Planck2015 results”. In: *Astronomy & Astrophysics* 594 (Sept. 2016), A13. DOI: 10.1051/0004-6361/201525830 (p. 5).
- [Pau] Wolfgang Pauli. “Pauli letter collection: letter to Lise Meitner”. Typed copy (p. 3).
- [Pic+92] A. Picard et al. “A solenoid retarding spectrometer with high resolution and transmission for keV electrons”. In: *Nuclear Instruments and Methods in Physics Research Section B: Beam Interactions with Materials and Atoms* 63.3 (Feb. 1992), pp. 345–358. DOI: 10.1016/0168-583x(92)95119-c (p. 8).
- [Pon58] B. Pontecorvo. “Inverse beta processes and nonconservation of lepton charge”. In: *Sov. Phys. JETP* 7 (1958). [*Zh. Eksp. Teor. Fiz.*34,247(1957)], pp. 172–173 (p. 4).

- [Raf+07] Adrian E. Raftery et al. “Estimating the integrated likelihood via posterior simulation using the harmonic mean identity”. In: *Bayesian Statistics*. 2007, pp. 1–45 (p. 16).
- [Sch+13] Magnus Schlösser et al. “Accurate calibration of the laser Raman system for the Karlsruhe Tritium Neutrino Experiment”. In: *Journal of Molecular Structure* 1044 (July 2013), pp. 61–66. DOI: 10.1016/j.molstruc.2012.11.022 (p. 13).
- [Sch18] Oliver Schulz. *BAT-2 Status*. BAT Meeting Max Planck Institute for Physics. Feb. 2018 (p. 18).
- [Sle15] Martin Slezák. “Monitoring of the energy scale in the KATRIN neutrino experiment”. PhD thesis. Nuclear Physics Institute, Czech Academy of Sciences, Nov. 2015 (pp. 18, 22, 37).
- [SK18] Martin Slezák and Christian Karl. *Fitness Studio and Fitrium: Code introduction*. URL: [https://neutrino.ikp.kit.edu/katrin/images/0/03/FitnessStudio\\_and\\_Fitrium.pdf](https://neutrino.ikp.kit.edu/katrin/images/0/03/FitnessStudio_and_Fitrium.pdf). KATRIN Hackathon Munich 2018. Aug. 2018 (p. 23).
- [Tan+18] M. Tanabashi et al. “Review of Particle Physics”. In: *Physical Review D* 98.3 (Aug. 2018). DOI: 10.1103/physrevd.98.030001 (p. 5).
- [Val06] K. Valerius. “Electromagnetic design and inner electrode for the KATRIN main spectrometer”. In: *Progress in Particle and Nuclear Physics* 57.1 (July 2006), pp. 58–60. DOI: 10.1016/j.pnpnp.2005.11.011 (p. 8).
- [Vén+18] D. Vénos et al. “Properties of 83mKr conversion electrons and their use in the KATRIN experiment”. In: *Journal of Instrumentation* 13.02 (Feb. 2018), T02012–T02012. DOI: 10.1088/1748-0221/13/02/t02012 (p. 21).
- [Wei12] Martin D. Weinberg. “Computing the Bayes Factor from a Markov Chain Monte Carlo Simulation of the Posterior Distribution”. In: *Bayesian Analysis* 7.3 (Sept. 2012), pp. 737–770. DOI: 10.1214/12-ba725 (p. 15).

## Acknowledgements

This thesis would not have been possible if not for the help and support of others.

I want to thank:

- Susanne Mertens, for offering me this highly interesting research opportunity and the environment I got to work in for the past year, for giving me the benevolent possibility of doing a research trip to Berkeley Lab, and for her consultation and support,
- Martin Slezák for his endless help and advice about physics, programming, and statistics, and developing the Fitness Studio, without which this thesis could not have been done,
- Alan Poon for giving me a warm and welcome, and also educating stay in Berkeley,
- Allen Caldwell for his many sessions of discussion and advice about Bayesian analysis,
- Oli Schulz for his support in the Bayesian Analysis Toolkit, the center piece of this work,
- Christian Karl for developing the Fitrium software, which much of this work depends on,
- Jan Balewski and the people at the NERSC for their support and information while I was in Berkeley,
- the KATRIN/TRISTAN group in the MPP container for being a warm and delightful community to work with, for many discussions about physics, but also fun times,
- my wonderful girlfriend Mikayla Webster, who has been supportive of me throughout my whole thesis work,
- and of course my family, who has been supporting me throughout my life, without whom I wouldn't be here.

We acknowledge the support of the Max Planck Institute for Physics and the resources of the National Energy Research Scientific Computing Center (NERSC), a U.S. Department of Energy Office of Science User Facility operated under Contract No. DE-AC02-05CH11231.